JGR Solid Earth

RESEARCH ARTICLE
10.1029/2025JB033029

Determining the Character of Subglacial Sediments in the Ice-Bedrock Interface Zone of Antarctica Using Horizontal-to-Vertical Spectral Ratios (HVSRs) of Seismic Ambient Noise

I. D. Kelly[1,2], A. M. Reading[1,2], T. Stål[1,2], B. Kulessa[2,3], A. García-Jerez[4], J. Piña-Flores[5], E. Paolucci[6], A. Tanzini[7], R. J. Turner[1], J. C. Magyar[1,2], and A. P. Bassom[1]

[1]School of Natural Sciences (Mathematics and Physics), University of Tasmania, Hobart, TAS, Australia, [2]Australian Centre for Excellence in Antarctic Science, Hobart, TAS, Australia, [3]School of Biosciences, Geography and Physics, Swansea University, Swansea, UK, [4]Departamento de Química y Física, Universidad de Almería, Almería, Spain, [5]Instituto de Ingeniería, Universidad Veracruzana, Vera Cruz, Mexico, [6]Department of Physics and Astronomy, University of Bologna, Bologna, Italy, [7]Department of Physics, Earth and Environmental Sciences, University of Siena, Siena, Italy

Key Points:

- HVSRs of seismic ambient noise can detect subglacial low-velocity zones formed either by unlithified sediments or water saturated rocks
- Seasonal increases in HVSR amplitudes across Antarctica are inversely correlated to sea ice extent in the Southern Ocean
- The presence and distribution of subglacial sedimentary basins in Antarctica is updated along major passive seismic transects

Supporting Information:

Supporting Information may be found in the online version of this article.

Correspondence to:

I. D. Kelly,
ian.kelly@utas.edu.au

Citation:

Kelly, I. D., Reading, A. M., Stål, T., Kulessa, B., García-Jerez, A., Piña-Flores, J., et al. (2026). Determining the character of subglacial sediments in the ice-bedrock interface zone of Antarctica using horizontal-to-vertical spectral ratios (HVSRs) of seismic ambient noise. *Journal of Geophysical Research: Solid Earth*, *131*, e2025JB033029. https://doi.org/10.1029/2025JB033029

Received 19 SEP 2025
Accepted 15 MAY 2026

Author Contributions:

Conceptualization: I. D. Kelly
Data curation: I. D. Kelly, T. Stål
Formal analysis: I. D. Kelly
Funding acquisition: A. M. Reading
Investigation: I. D. Kelly
Methodology: I. D. Kelly
Project administration: A. M. Reading
Software: I. D. Kelly, A. García-Jerez, J. Piña-Flores, E. Paolucci, A. Tanzini
Supervision: A. M. Reading, T. Stål, A. P. Bassom
Validation: I. D. Kelly, A. García-Jerez, J. Piña-Flores, E. Paolucci, A. Tanzini, R. J. Turner

Abstract Interactions between the Antarctic Ice Sheet and the underlying solid Earth occur within the ice-bedrock interface zone (IBIZ), containing structures of sediments and rocks that strongly influence ice sheet dynamics. Existing insights into the Antarctic IBIZ come primarily from interpretations of airborne geophysical data and active seismic measurements, which require significant logistics. Passive seismic methods provide a lower cost, lower resolution alternative for subglacial mapping, with the potential for continuous remote monitoring. Here, we utilize horizontal-to-vertical spectral ratios (HVSRs) of seismic ambient noise to infer the presence of subglacial low-velocity zones generated by unlithified sediments or porous, water saturated sedimentary rocks, using existing data from over 80 broadband stations across Antarctica. From 1-D forward modeling, we identify a decrease in synthetic HVSR peak frequencies dependent on the thickness and S-wave velocity (V_S) of the low-velocity zone unrelated to seismic wavefield conditions. This sensitivity in HVSR peak frequencies is validated by the agreement between synthetic and observed HVSRs at Antarctic stations with independent prior constraints on subglacial structure. Our observed HVSR analysis additionally reveals a widespread seasonality in observed HVSR amplitudes between 0.2 and 1 Hz that correlates with sea ice evolution and the modulation of secondary microseism energies in the Southern Ocean. From the decrease in observed HVSR peak frequencies, we infer the likelihood of subglacial low-velocity zones across Antarctica along major passive seismic transects, mapping to key subglacial sedimentary basins. We provide practical recommendations for future HVSR applications to infer subglacial low-velocity zones reliably.

Plain Language Summary The Antarctic Ice Sheet flows continuously toward and into the surrounding ocean, where it calves and melts. The movement of ice depends on the connection between the ice and underlying rocks: specifically, the presence of loose sediments or weak, water saturated rocks allows ice to slide more easily than when it is in direct contact with solid bedrock. Mapping such sediments and rocks within this "ice-bedrock interface zone" will therefore improve our understanding of current ice sheet behavior and help us to better predict Antarctica's future evolution and contributions to global sea levels. However, with ice covering >99% of the continent and averaging over 2 km in thickness, direct access to the bed is impractical. Here, we show that background seismic signals generated by ocean waves, known as seismic ambient noise, can be used to detect the "low-velocity zones" created by these sediments and rocks beneath the ice sheet. We apply this method across Antarctica, finding low-velocity zones in key areas. Importantly, this analysis only requires a single sensor and a few hours of recording, encouraging rapid field deployments and improved coverage across the remote Antarctic interior.

1. Introduction

The polar ice sheets have experienced widespread and sustained mass losses over recent decades (Otosaka et al., 2023; Rignot et al., 2019; Velicogna et al., 2020). In particular, the Antarctic Ice Sheet (AIS) presents the major potential contributor to future global sea level rise (Millan et al., 2022) and accurate projections of how the AIS will continue evolving remains an exigent concern (Constable et al., 2022). Substantial uncertainties exist in

Visualization: I. D. Kelly, T. Stål, R. J. Turner
Writing – original draft: I. D. Kelly
Writing – review & editing: I. D. Kelly, A. M. Reading, T. Stål, B. Kulessa, A. García-Jerez, J. Piña-Flores, E. Paolucci, A. Tanzini, R. J. Turner, J. C. Magyar, A. P. Bassom

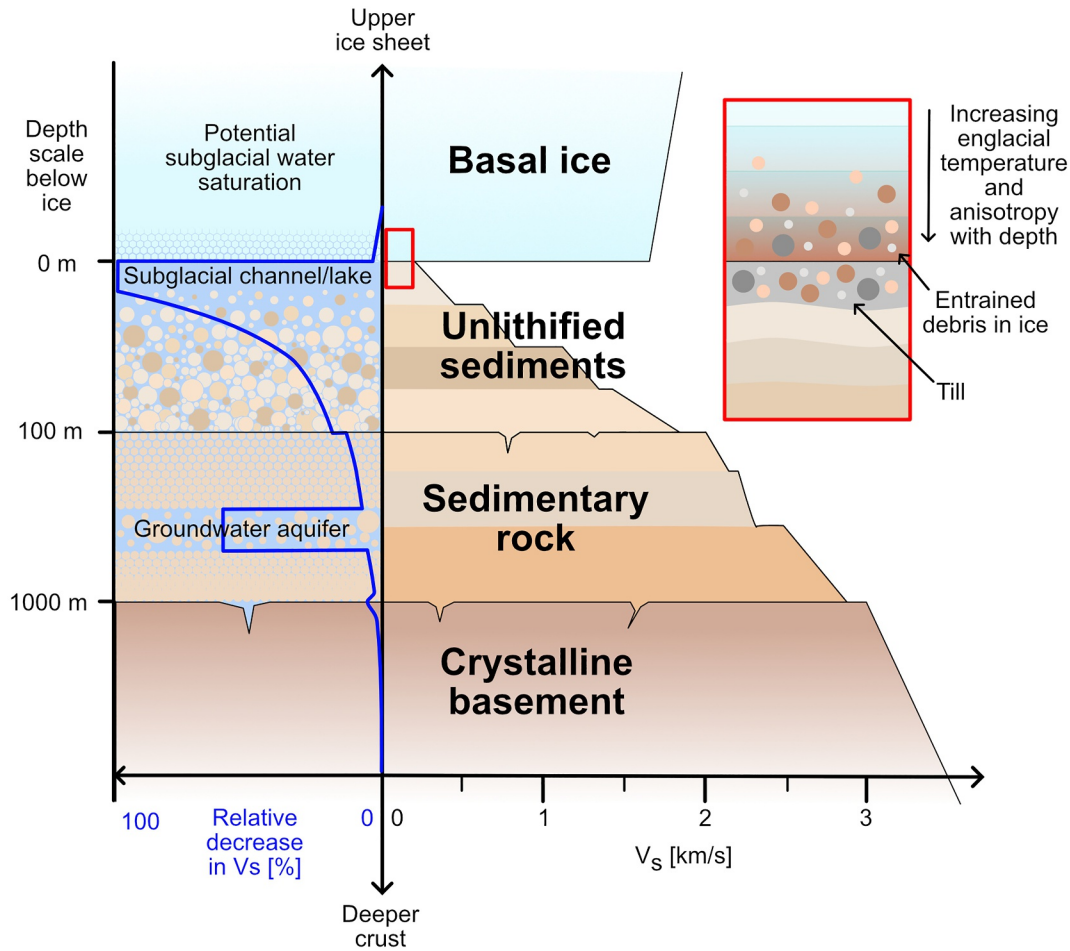

Figure 1. Diagram illustrating the structures of basal ice, unlithified sediments, sedimentary rocks and crystalline basement that comprise the IBIZ. Characteristic ranges in V_S and evolutions with depth (e.g., Mavko et al., 2020; Schön, 2015) are displayed alongside the superposing influence of subglacial water (e.g., Toksoz et al., 1976), which decreases V_S depending on the saturation content and introduces additional structural complexity into the IBIZ. The red inset highlights the smaller-scale variability at the ice-bed contact, such as the presence of till, inclusion of debris in the basal ice, anisotropic ice fabric, and englacial temperature gradients (Section 1).

current estimates of global sea level rise from ice sheet modeling, in large part associated with the coupling between the AIS and the underlying solid Earth (Fyke et al., 2018; Ritz et al., 2015). This ice-bedrock interface zone (IBIZ) hosts several mechanisms consequential to ice sheet dynamics and long-term mass balance, including basal deformation and sliding (Koellner et al., 2019; McCormack et al., 2022), glacial isostatic adjustment (Whitehouse et al., 2019), geothermal heat flow (Reading et al., 2022), subglacial hydrology (Ashmore & Bingham, 2014) and groundwater dynamics (Li et al., 2022). A capability to better understand and monitor these mechanisms is therefore a key priority as the scientific community works toward constraining future AIS evolution (Fricker et al., 2025; Noble et al., 2020; Pattyn & Morlighem, 2020).

Structurally, the Antarctic IBIZ consists of a diverse composition of ice, water, sediments and rocks (Figure 1). Basal ice can be close to the pressure-melting point (Dawson et al., 2022, 2024), strongly anisotropic in its crystal orientation fabric (Diez & Eisen, 2015; Diez et al., 2015) and contain significant amounts of entrained debris (Franke et al., 2023; Winter et al., 2019). The underlying geology is heterogeneous over a continental scale, but can be broadly described by a crystalline basement overlain in some regions by sedimentary rocks in subglacial sedimentary basins (Aitken et al., 2023), and/or by thinner layers of unlithified sediments, including till (Evans et al., 2006). Meltwater can permeate the subglacial material, forming a network of channels and lakes (Dow, 2022; Livingstone et al., 2022) as well as deeper groundwater aquifers (Aitken et al., 2023; Li et al., 2022).

Insights into the Antarctic IBIZ come predominantly from geophysical surveying, with sub-ice drilling for direct observations remaining costly and logistically challenging despite ongoing technological developments (Gong et al., 2019; Goodge et al., 2021; Kuhl et al., 2021). Airborne radio-echo sounding (RES) is used for mapping subglacial lakes and bed topography (Schroeder et al., 2020), supplying the primary source data for gridded ice thickness products such as Bedmap (Fretwell et al., 2013; Pritchard et al., 2025) and BedMachine (Morlighem et al., 2020). The simultaneous collection of gravity and magnetic anomaly data (MacGregor et al., 2021) informs tectonic structure (e.g., Aitken et al., 2014; Jordan et al., 2023) and enables the coarse delineation of subglacial sedimentary basins (e.g., Aitken et al., 2016; Frederick et al., 2016). Magnetotellurics has demonstrated the potential to infer the presence of subglacial groundwater (Gustafson et al., 2022). Meanwhile, reflection seismics can reveal both englacial and subglacial horizons at high resolution (e.g., Horgan et al., 2011; Muto et al., 2019) and allows for thin, dilatant till layers to be distinguished and correlated to areas of high ice velocities (e.g., Brisbourne et al., 2017; Kulessa et al., 2017).

Passive seismic methods have been adopted in recent years to provide alternatives to subglacial imaging without the need for active sources. Notably, receiver functions of earthquakes (Langston, 1977), exploiting the conversion of teleseismic arrivals at subsurface contrasts in S-wave velocity (V_S), have inferred thick (>100 m), low-V_S (<1,000 m/s) units beneath the polar ice sheets (Anandakrishnan & Winberry, 2004; Chaput et al., 2014; Dunham et al., 2020; Walter et al., 2014). Low-velocity zones formed either by unlithified sediments or porous, water saturated sedimentary rocks between the ice and basement (Figure 1) shift the dominant V_S contrast from the ice-bed interface to the subglacial basement interface, causing an arrival delay in the receiver function that can be used to constrain subglacial layer thickness and average V_S (Anandakrishnan & Winberry, 2004). The need for a reasonable number of suitable events typically necessitates teleseismic data collection over at least several weeks for reliable interpretations; in comparison, the use of ambient seismic noise (Nakata et al., 2019) enables measurements over daily timescales and the opportunity to detect inter-annual and seasonal subsurface variations (e.g., Mordret et al., 2016; Zhan, 2019).

Horizontal-to-vertical spectral ratios (HVSRs) provide a practical analysis of seismic ambient noise for determining the depth of subsurface V_S discontinuities (Molnar et al., 2022). From the simple computation of the ratio between the horizontal- and vertical-component Fourier spectra at a single three-component station, bedrock depths across sedimentary basins can be mapped from recordings of only several minutes (e.g., Farazi et al., 2023; García-Jerez et al., 2006; Mulargia & Castellaro, 2016; Paolucci et al., 2015). HVSRs have been similarly utilized to estimate ice thicknesses across a range of glacial settings (e.g., Fu et al., 2023; Köhler et al., 2019; Picotti et al., 2017; Stevens et al., 2023). Over the AIS however, Yan et al. (2018) found varying discrepancies between HVSR estimates of ice thickness and Bedmap2 (Figure 2), which were attributed to a widespread low-velocity layer in the basal ice (Wittlinger & Farra, 2012, 2015). The proposed ∼25% decrease in englacial V_S within this low-velocity layer has since been shown to require an unrealistic amount of meltwater within the crystalline ice matrix (Llorens et al., 2020). Considering the spatial correlation of these discrepancies to subglacial sedimentary basins (Figure 2a) and aligning with receiver function interpretations, an alternative explanation to these discrepancies is the presence of subglacial low-velocity zones generated by unlithified sediments or porous, water saturated sedimentary rocks.

The potential of HVSRs to track subsurface V_S changes has been recently highlighted in the context of groundwater dynamics (Rigo et al., 2021; Seivane et al., 2022), seasonal permafrost thawing (Köhler & Weidle, 2019; Kula et al., 2018), and subglacial water drainage (van Ginkel et al., 2025). However, this potential can be complicated by the influence of varying wavefield conditions (e.g., Benkaci et al., 2021; Chatelain et al., 2008; Guillier et al., 2007). In Antarctica, low-frequency wavefield variability is largely driven by the seasonal modulation in primary (0.05–0.1 Hz) and short-period secondary (0.2–1 Hz) ocean microseism energies by sea ice cover (Sergeant et al., 2013; Stutzmann et al., 2009; Tsai & McNamara, 2011). Primary microseisms are generated by the direct forcing of ocean gravity waves on the seafloor in shallow water, predominantly along the continental slope (Gualtieri et al., 2019; Hasselmann, 1963). Short-period secondary microseisms are attributed to pressure fluctuations on the seafloor caused by the interaction between incoming and coastal-reflected ocean gravity waves (Ardhuin et al., 2011; Longuet-Higgins & Jeffreys, 1950; Yang & Ritzwoller, 2008). The presence of sea ice inhibits the formation of these coastal microseism sources (Stutzmann et al., 2012), resulting in a consistent anti-correlation between sea ice extent and single-component seismic noise levels within 0.05–0.1 and 0.2–1 Hz across Antarctica (Anthony et al., 2015, 2017; Grob et al., 2011; Pratt et al., 2017; Turner et al., 2020). Furthermore, azimuthal HVSR variability can exist due to several factors (Cheng et al., 2020) including non-

10.1029/2025JB033029

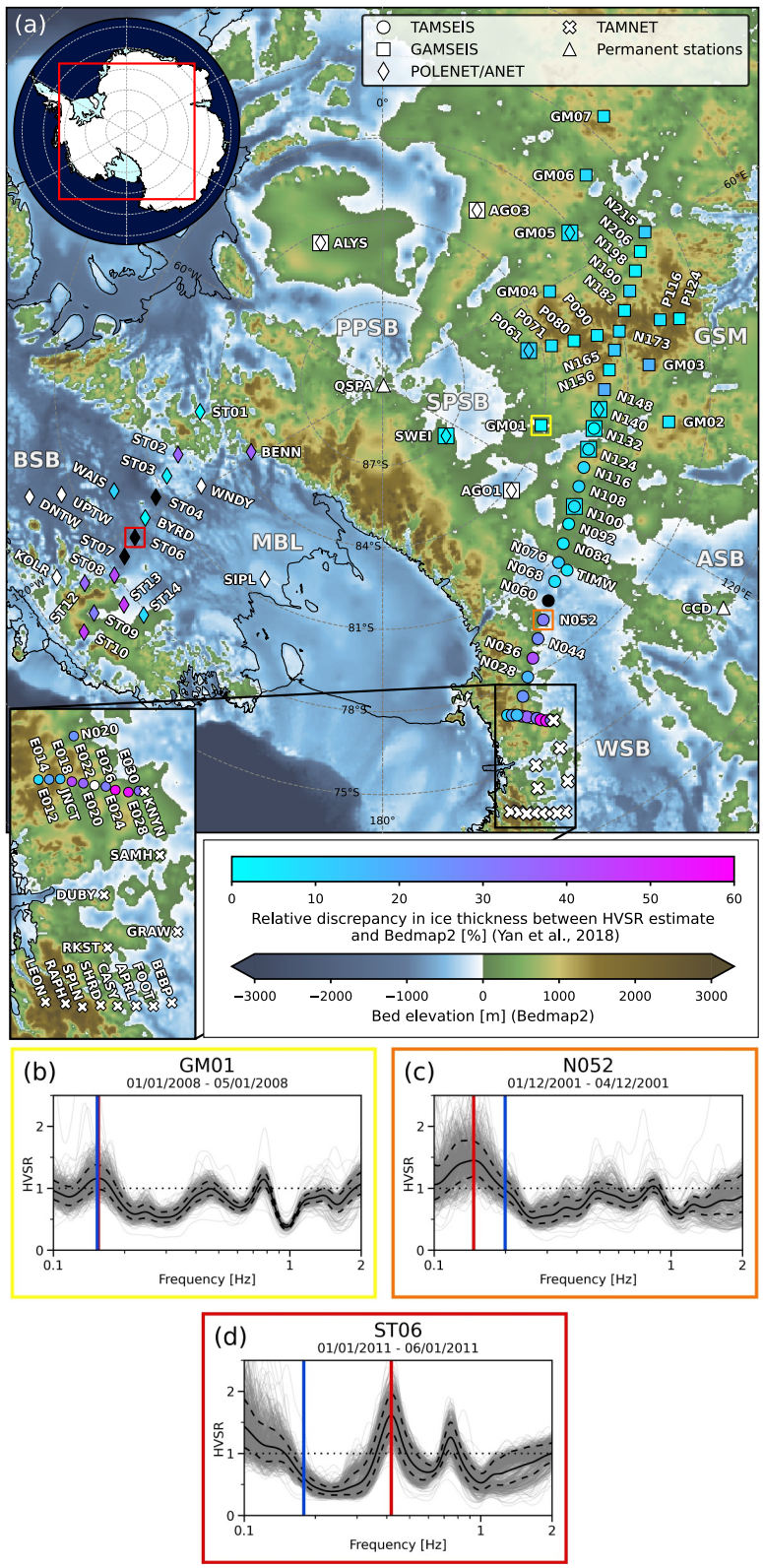

Figure 2.

planarity in the basement topography (e.g., Matsushima et al., 2014, 2017), which can distort HVSR interpretations based on horizontal-component averaging (Molnar et al., 2022). Non-planar basement topography and varying wavefield conditions could therefore complicate the potential of HVSRs to monitor key changes in sub-ice sheet conditions, for instance, caused by groundwater discharge (Cairns et al., 2025; Li et al., 2022; Robel et al., 2023) or rapid bed erosion (Smith et al., 2007, 2012).

In this study, we determine the potential of HVSR analysis to infer the presence of subglacial low-velocity zones formed by unlithified sediments or porous, water saturated sedimentary rocks and enable low cost insights into the Antarctic IBIZ (Figure 1). We first explore the sensitivity of synthetic HVSRs to subglacial low-velocity zones through systematic 1-D forward modeling, testing a broad range of plausible configurations for the Antarctic subsurface and comparing modeling algorithms assuming different wavefield mechanisms. We then newly compute and analyze observed HVSRs for over 80 stations across the AIS (Figure 2) to compare with our forward modeling and assess the spatiotemporal consistency of observed HVSRs in Antarctica. From these observed HVSRs, we interpret the presence of subglacial low-velocity zones beneath the analyzed stations and make practical recommendations for the future application of HVSRs to map and potentially monitor sub-ice sheet conditions.

2. Methods and Data

2.1. Theoretical Background of HVSRs

The underlying interpretation of HVSRs relates the frequencies of observed peaks (f_n^{obs}) to the resonance frequencies (f_n) of the S-wave transfer function for a 1-D subsurface profile defined by a uniform layer of thickness h and V_S overlying a half-space (Molnar et al., 2022):

$$f_n = (2n+1)\frac{V_S}{4h}, \quad (n = 0, 1, 2, \dots). \tag{1}$$

Investigations have consistently matched the dominant, lowest-frequency HVSR peak (f_0^{obs}) to the fundamental resonance frequency (f_0) expected for the substation bedrock depth (e.g., Haghshenas et al., 2008; Parolai et al., 2002, 2023), assuming the subsurface structure can be treated as 1-D (Cheng et al., 2020) and the peak does not arise from noise sources immediately local to the sensor (Benkaci et al., 2021; Chatelain et al., 2008).

Interpretations of f_0^{obs} remain robust to the recorded wavefield, whether composed of stationary or non-stationary noise sources (e.g., Bonnefoy-Claudet, Cotton, & Bard, 2006; Guillier et al., 2007; Parolai et al., 2009), earthquake events (e.g., Kawase et al., 2018; Mucciarelli et al., 2003; Parolai et al., 2004) or even active seismic sources (Mi et al., 2019). Ambiguity has thus emerged surrounding the physical mechanisms underpinning HVSR interpretations and resulted in a variety of forward models being developed (Lunedei & Malischewsky, 2015; Molnar et al., 2022). Nakamura (1989) initially proposed a total equivalence between the S-wave transfer function and HVSRs, allowing both f_0 and the corresponding site amplification factor to be yielded respectively from f_0^{obs} (i.e., Equation 1) and the amplitude of the fundamental peak. Support for such HVSR interpretations of vertically

Figure 2. (a) Map of the on-ice broadband seismometers in Antarctica considered in this study. Station markers indicate the Trans-Antarctic Mountains Seismic Experiment (TAMSEIS; Lawrence et al., 2006), Trans-Antarctic Mountains Northern Network (TAMNET; Hansen et al., 2015), Gamburtsev Antarctic Mountains Seismic Experiment (GAMSEIS; Hansen et al., 2010), Polar Earth Observing Network/Antarctic Network (POLENET/ANET; Chaput et al., 2014), and the permanent stations installed at Concordia (CCD; Bès de Berc et al., 2023) and the Quiet South Pole Observatory (QSPA; Anthony et al., 2021). The majority of stations are color-mapped according to the relative discrepancy in substation ice thickness between values estimated by Yan et al. (2018) from observed HVSR peak frequencies (i.e., f_0 from Equation 1, assuming V_S = 1,900 m/s for ice) and Bedmap2 (Fretwell et al., 2013). Other station markers denote those excluded from further analysis by Yan et al. (2018) due to the relative discrepancy in substation ice thickness being too large (black), and those not included in their study (white). Shown as a background is the corresponding bed elevation from Bedmap2, highlighting the major subglacial sedimentary basins (BSB, Byrd Subglacial Basin; PPSB, Pensacola-Pole Subglacial Basin; SPSB, South Pole Subglacial Basin; WSB, Wilkes Subglacial Basin; ASB, Aurora Subglacial Basin), as well as other key regions (MBL, Marie Byrd Land; GSM, Gamburtsev Subglacial Mountains). Sub-plots (b, c and d) display example observed HVSRs for the different interpretations made by Yan et al. (2018), with border colors (yellow, orange, red) matching the symbol highlighting their location in the above map: (b) GM01, where estimated and expected ice thickness values were consistent; (c) N052, where a significant discrepancy is noticed; and (b) ST06, which was excluded from further analysis. The vertical red and blue lines in (b, c and d) illustrate respectively the frequency of HVSR peaks selected by Yan et al. (2018) and the expected f_0 for the Bedmap2 substation ice thickness. The solid gray, solid black, and dashed black lines respectively denote the HVSRs from each accepted window (Text S1 in Supporting Information S1), the resulting mean HVSR, and the standard deviation in the mean HVSR. The horizontal dotted black line indicates HVSR values of unity.

propagating body-wave resonance (BWR) has persisted (Nakamura, 2019; Oubaiche et al., 2016), despite widely recognized inconsistencies in the amplitude relationship (e.g., Bard, 1999; Field & Jacob, 1993; Lachet & Bard, 1994). Considering the dominance of Rayleigh waves in ambient noise (Bonnefoy-Claudet, Cotton, & Bard, 2006), f_0^{obs} is more commonly related to peaks in the fundamental-mode Rayleigh-wave ellipticity (RWE; Fäh et al., 2001; Konno & Ohmachi, 1998; Nogoshi & Igarashi, 1971). More recently, full-wavefield approaches have been developed to assimilate both body- and surface-wave contributions, either by adopting a diffuse field assumption (DFA; Kawase et al., 2015; Sánchez-Sesma et al., 2011) or through modeling a distribution of surface sources (DSS) around the sensor (Lunedei & Albarello, 2009, 2010, 2015, 2021).

Regardless of the assumed model, f_0^{obs} can be consistently predicted for normally dispersive velocity profiles, despite significant discrepancies in the fundamental peak amplitude (Albarello et al., 2023; Bonnefoy-Claudet, Cornou, et al., 2006). However, the performance and consistency of HVSR forward models when a low-velocity zone exists is poorly known. Studies of dispersion curve behavior highlight dominant contributions from higher surface-wave modes with increasing frequency when a low-velocity zone is present (Dou & Ajo-Franklin, 2014; Foti et al., 2018; Mi et al., 2018), which have the potential to promote the excitation of higher-mode HVSR peaks (i.e., $n > 0$, Equation 1). Secondary peaks above f_0^{obs} are typically interpreted to arise from shallower discontinuities (Molnar et al., 2022), likely due to the strong attenuation properties of surficial sediments (Toksöz et al., 1979). In contrast, glacial ice presents a homogeneous, weakly attenuating medium (Peters et al., 2012) that supports multi-mode resonance patterns in teleseismic signals (Zhang & Olugboji, 2023). Higher-mode surface-wave energies may therefore offer an alternative explanation to secondary peak features observable in Antarctic HVSRs (Figure 2), aligning with interpretations of RWE over the Greenland Ice Sheet (Jones et al., 2023). Consequently, a forward modeling approach that can simulate both fundamental and higher-mode peak behavior under the influence of a low-velocity zone is required.

2.2. Forward Modeling of Synthetic HVSRs

To investigate HVSR sensitivity under different wavefield mechanisms, we employ the algorithms provided by Albarello et al. (2023) to model and compare synthetic HVSRs from the BWR, RWE, DFA and DSS models (Table S1 in Supporting Information S1). For all cases, HVSRs are modeled within the frequency range of 0.01–5 Hz for 1-D profiles consisting of a series of layers with thickness h overlying a half-space, each defined by a uniform V_S, P-wave velocity V_P and density ρ. Seismic attenuation is also incorporated in the BWR and DSS algorithms through quality factors Q_S and Q_P, although alongside other parameterization differences (e.g., wavefield components, number of surface-wave modes), this causes a variability in HVSR amplitudes between models and limits inter-model comparisons to the frequency domain (Albarello et al., 2023). Other algorithm settings are kept as per Albarello et al. (2023), with the exception of the source correlation range d_j in the full-wavefield implementation of the DSS model, which is increased to artificially enhance higher-mode peaks (Lunedei & Albarello, 2015).

We henceforth use the BWR model to exemplify synthetic HVSR behavior in our study (Text S2 in Supporting Information S1). Shallow profile tests isolating modal RWE (Figure S1 in Supporting Information S1) and different surface-wave components in the DFA and DSS models (Figure S2 in Supporting Information S1) identify numerical irregularities that emerge at higher frequencies when a low-velocity zone is introduced, related to higher-mode surface-wave contributions and preventing the characterization of higher-mode HVSR peaks. This is attributed to the modal summation calculation used in these algorithms to determine modal surface-wave branches (Aki & Richards, 2002), which can fail for inversely dispersive profiles (Wathelet, 2008). Nevertheless, we find the synthetic fundamental peak frequency (f_0^{syn}) to be consistent between these models and the BWR model despite differences in amplitude behavior, supporting the conclusions of Albarello et al. (2023). Moreover, further testing (Text S2 in Supporting Information S1) provides strong evidence that in the absence of numerical irregularities, both higher surface-wave modes and higher BWR modes can explain higher-mode peak frequencies in the synthetic HVSRs ($f_{n>0}^{\text{syn}}$). We therefore select the BWR model to represent the wavefield-independent behavior of both fundamental and higher-mode HVSR peak frequencies, ensuring a consistency with other wavefield mechanisms by comparing synthetic HVSRs from the fundamental-mode RWE and full-wavefield representations of the DSS and DFA models in the supplement.

We apply these algorithms to generate synthetic HVSRs for "simple-case" profiles describing the Antarctic subsurface by a single subglacial layer (with thickness h_l and S-wave velocity $V_{S,l}$) between a uniform ice sheet (with thickness h_i and S-wave velocity $V_{S,i}$ = 1,900 m/s) and basement half-space, similar to previous studies (Anandakrishnan & Winberry, 2004; Chaput et al., 2014; Dunham et al., 2020; Phạm & Tkalčić, 2018). For the subglacial layer, we make the additional distinction between unlithified sediments and sedimentary rocks, defining separate parameter ranges for the two scenarios by combining present knowledge of Antarctic subsurface structure with viscoelastic properties assumed from rock physics (Text S3 and Table S2 in Supporting Information S1). Our parameter choices are further supported by sensitivity tests for V_P, ρ, Q_S, Q_P and the basement V_S (Figures S3–S7 in Supporting Information S1).

We also perform forward modeling for several "complex-case" end-member scenarios to explore if HVSR behavior is complicated by more realistic variability in the ice sheet and underlying geology (Figure 1). These scenarios separately consider (Text S4 in Supporting Information S1): (a) the presence of a surficial firn layer (van den Broeke, 2008; Pearce et al., 2023, 2024); (b) depth-wise evolution in ice sheet properties due to englacial temperature, ice fabric anisotropy, and debris entrainment (Franke et al., 2023; Llorens et al., 2020), and (c) additional layering and gradual consolidation with depth in the subglacial material.

2.3. Data and Processing of Observed HVSRs

For our observed HVSR analysis, we initially consider all stations shown in Figure 2, comprising the majority of broadband seismometers available on the AIS (excluding ice shelf stations). Data consistency and quality were found to vary significantly between these stations, leading to a total of 82 stations being selected for HVSR analysis (Text S5 in Supporting Information S1). We compute observed HVSRs (Text S1 in Supporting Information S1) for each selected station over time series of 5 days with window lengths of 600 s, similar to Yan et al. (2018), although use the *hvsrpy* package (Vantassel, 2025) for data processing and window rejection (Cox et al., 2020).

At most stations, we extend HVSR analysis over a selected yearly period of good-quality data to assess the influence of the seasonal modulation in ocean microseism energies by sea ice cover (Section 1). This excludes the 22 stations within the TAMSEIS network, where available recordings are restricted to the austral summer (Text S5 in Supporting Information S1). We additionally quantify azimuthal HVSR variability using *hvsrpy* by interpolating our observed HVSRs across the separate horizontal components into 2-D surface plots (Cheng et al., 2020).

3. Results

3.1. Sensitivity of Synthetic HVSR Peak Frequencies

Figures 3 and 4 summarize synthetic HVSR behavior for the two simple-case scenarios with a single subglacial layer of either unlithified sediments or sedimentary rocks. In both cases, we observe a downwards shift in all synthetic peak frequencies (f_n^{syn}) dependent on the subglacial low-velocity zone defined relative to h_i, scaling with h_l and inversely with $V_{S,l}$. A low-velocity zone exists for all unlithified sediment $V_{S,l}$, resulting in a smooth transition in f_0^{syn} as h_l increases and $V_{S,l}$ decreases, as well as an amplification in the fundamental peak. For a sedimentary rock layer, the shifted fundamental peak can only be clearly distinguished from that of an ice-basement interface when $V_{S,l} \leq V_{S,i}$ (relating to porous or water saturated sedimentary rocks). With peak frequency shifting consistent for f_0^{syn} between the different models (Figures S8–S15 in Supporting Information S1), we interpret a wavefield-independent mechanism arising from low-velocity subglacial material refining the dominant subsurface V_S contrast, similar to the arrival delay observed in receiver functions (Section 1). Conversely, we find that synthetic HVSR amplitudes vary greatly between the models (Figures S8–S15 in Supporting Information S1), as well as with parameters unrelated to subsurface V_S (Text S3 in Supporting Information S1).

The relative decrease in peak frequency caused by the presence of a subglacial low-velocity zone compared with an expected ice-basement interface (where $f_n^{\text{syn}} \approx f_n$) is potentially explained by the f_n relating to the effective average of layers above the half-space (f_n^{eff}), a metric commonly used to convert f_0^{obs} to sedimentary basin depths using borehole calibrations (Molnar et al., 2022). As an example, we compute f_n^{eff} for the lowest values of $V_{S,l}$ for

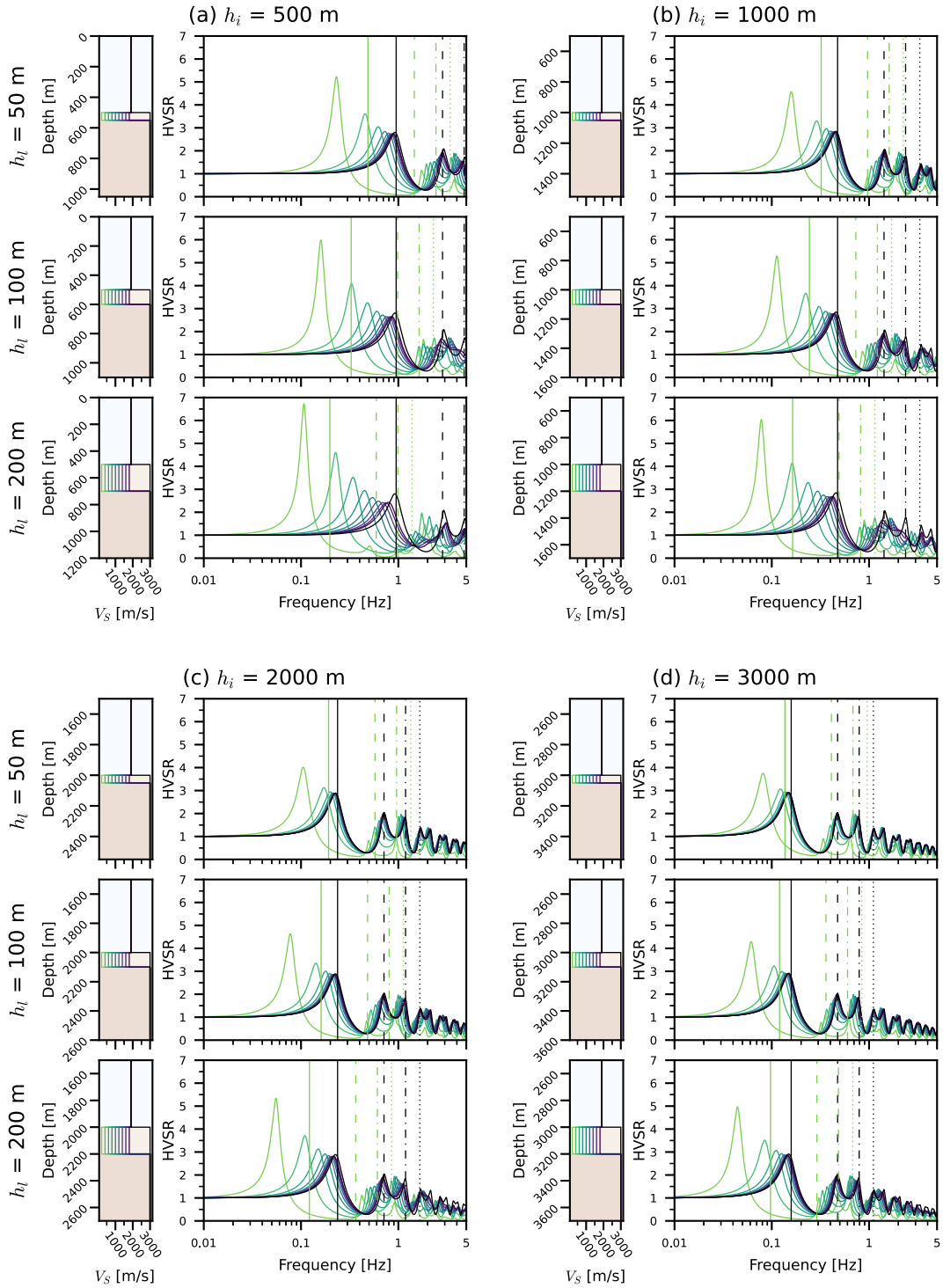

Figure 3. Synthetic HVSRs (from the BWR model) for the simple-case scenario of a single subglacial layer of unlithified sediments. Subplots (a–d) show synthetic HVSRs for a set h_i, with each row corresponding to a set h_l with varying $V_{S,l}$ as per Table S2 in Supporting Information S1. The vertical lines illustrate the f_n expected from an ice-basement interface (black lines) and the f_n^{eff} (Section 3.1) combining the ice and lowest-V_S subglacial layers (green lines), for $n = 0$ (solid lines), $n = 1$ (dashed lines), $n = 2$ (dashed-dotted lines), and $n = 3$ (dotted lines). Refer to Figures S8–S11 in Supporting Information S1 for the full set of synthetic HVSRs for this scenario, including an inter-model comparison.

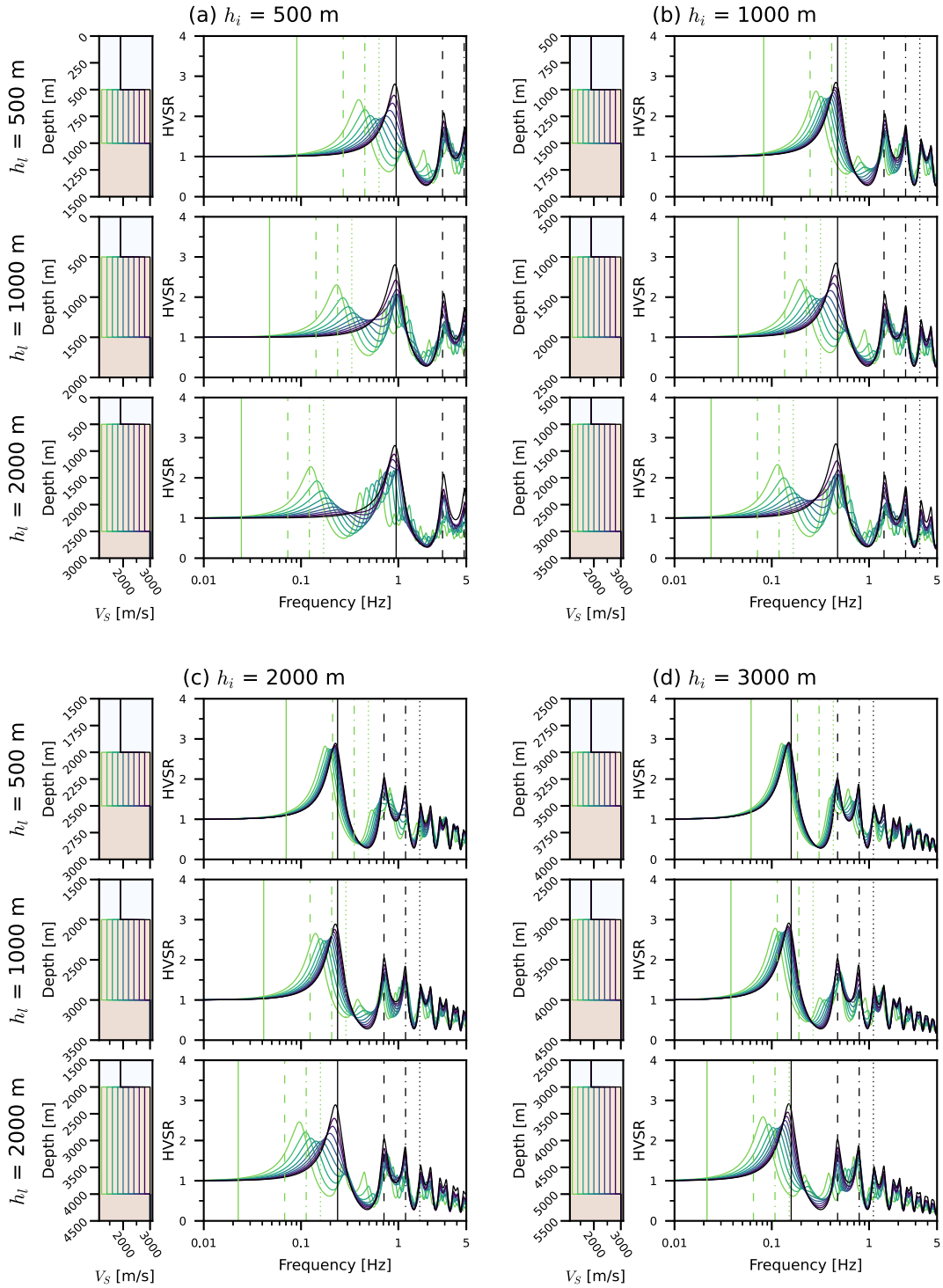

Figure 4. Synthetic HVSRs (from the BWR model) for the simple-case scenario of a single subglacial layer of sedimentary rocks. Refer to Figure 3 for plot details and to Figures S12–S15 in Supporting Information S1 for the full set of synthetic HVSRs for this scenario, including an inter-model comparison.

both subglacial layer scenarios (Figures 3 and 4) using the standard harmonic mean (Ibs-von Seht & Wohlenberg, 1999) of the ice and subglacial layers for f_n up to $n = 3$. For the layer of unlithified sediment (Figure 3), we find that f_0^{eff} underestimates f_0^{syn} for the lowest $V_{S,l}$, which is noticed for the other models (Figures S8–S11 in Supporting Information S1). The corresponding behavior in $f_{n>0}^{\text{syn}}$ appears to be less consistent for the unlithified

sediment scenario, with the synthetic higher-mode peaks appearing with weak amplitudes and lying above or below the corresponding f_n^{eff} depending on the combination of h_i and h_l (Figure 3). In contrast, we find the peak frequencies for the sedimentary rock layers to be well predicted by f_n^{eff} for all h_i and h_l (Figure 4), with a similar agreement between f_0^{syn} and f_0^{eff} for the other models (Figures S12–S15 in Supporting Information S1). For the sedimentary rock scenario, we also note that the envelope of synthetic HVSR amplitudes roughly matches with the synthetic HVSR generated from an ice-basement interface in many cases (Figure 4); for instance, for h_l = 2,000 m, the synthetic second higher-mode peak from the subglacial layer emerges at a comparable frequency to the first higher-mode peak predicted for an ice-basement interface (Figure 4c). This underlines the possibility to misinterpret the modes of observed HVSR peaks (e.g., Figure 2d), particularly when the fundamental peak is not clearly observed (Section 3.2).

Our complex-case end-member scenarios indicate that additional complexity in the Antarctic subsurface has minimal influence on peak frequency behavior. Incorporating a surficial firn layer (Figure S16 in Supporting Information S1) does not appreciably affect the $V_{S,i}$ profile and only generates HVSR peaks if the firn is treated as an unrealistic, uniformly low-V_S layer (Lévêque et al., 2010). Realistic heterogeneity in the glacial ice can also be ignored (Figure S17 in Supporting Information S1), with f_n^{syn} only discernibly affected by the low-velocity layer in the basal ice suggested by Yan et al. (2018). Meanwhile, additional layering or gradual consolidation in the subglacial material (Figures S18–S20 in Supporting Information S1) yields comparable f_n^{syn} to the synthetic HVSRs generated from a single subglacial layer. We therefore establish that the simple-case approximation of the IBIZ can be reliably used for HVSR interpretations, with peak frequencies being predominantly sensitive to the bulk presence of a subglacial low-velocity zone.

Our forward modeling results indicate that HVSRs can be used to infer the presence of subglacial low-velocity zones formed by either unlithified sediments or porous, water saturated sedimentary rocks from the decrease in f_n^{obs} relative to the f_n expected from an ice-basement interface, using substation ice sheet thicknesses given by gridded products (Section 1) and a reasonable assumption of ice sheet $V_S \approx$ 1,900 m/s. In this study, we additionally consider uncertainties in f_n (σ_{f_n}) by incorporating uncertainties in ice thickness estimates and plausible variations in ice sheet V_S between 1,800 and 2,000 m/s (Text S3 in Supporting Information S1) into Equation 1.

3.2. Sensitivity of Observed HVSR Peak Frequencies

We first compare synthetic and observed HVSRs at stations where subglacial structure has been independently constrained by previous receiver function inversions (Figure 5). This enables us to assess if the modeled sensitivity in HVSR peak frequencies (Section 3.1) has practical application for the interpretation of observed HVSRs. At the majority of sites (Figure 5), we see a clear relation between f_n^{obs} and f_n^{syn} up to $n = 2$, supporting our forward modeling results and confirming the observed higher-frequency peaks as higher-mode resonances from the basement half-space, rather than fundamental resonances from shallower discontinuities (Section 2.1). An excellent correspondence in the shape between the observed and synthetic HVSRs is found at several stations (e.g., GM01, ST04, ST06, ST09; Figure 5), especially against the DFA model for stations located toward the quiet continental interior (e.g., QSPA, N052, ST01; Figure S21 in Supporting Information S1). At some sites inferred to overlie subglacial low-velocity zones (e.g., ST04, ST06, UPTW; Figure 5), only the higher-mode peaks are observable, with the expected fundamental peak lost to incoherencies below 0.1 Hz likely associated with sensor tilt (Text S5 in Supporting Information S1). We note that our interpretations are independent of the characteristically weak HVSR amplitudes observed (e.g., QSPA; Figure S21 in Supporting Information S1), considering that synthetic and observed HVSR amplitudes are affected by a number of factors unrelated to subsurface V_S (Section 4.4).

Discrepancies between the synthetic and observed HVSRs at some stations (Figure 5) can be largely explained by improvements in RES data coverage and substation ice thickness estimates between the receiver function studies and more recent data sets such as BedMachine (Table 1). By computing f_n using substation ice thicknesses from BedMachine, we can reassess the subglacial structures interpreted at stations ST01, ST10 and ST13 by Chaput et al. (2014), where either an ice-basement interface or an unresolvable subglacial layer (Section 4.4) is indicated by the agreement between f_n^{obs} and the BedMachine f_n (Figure 5). Thinner subglacial layers are suggested at ST09 and UPTW, whilst the improved alignment between f_n^{obs} and the BedMachine f_n provides stronger evidence for an ice-basement interface at BYRD and ST03 (Figure 5). This highlights the importance of accurate ice thickness

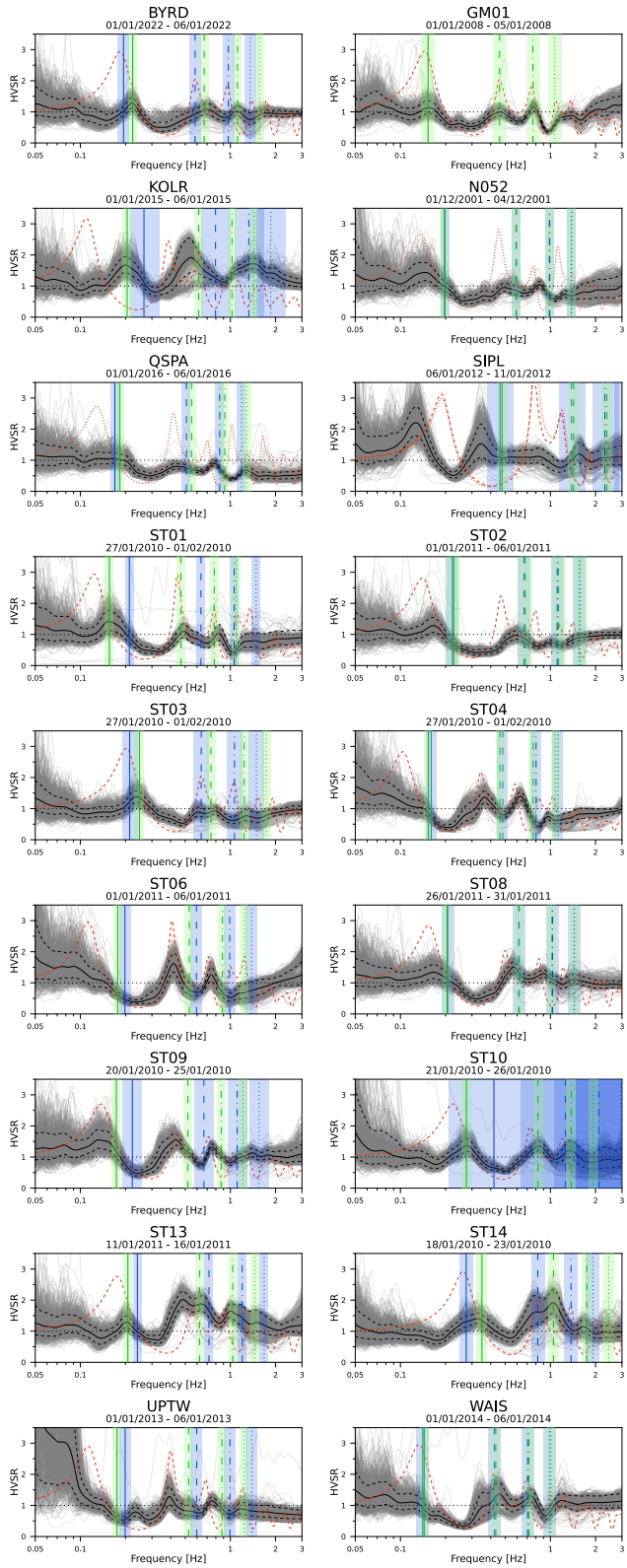

Figure 5.

estimates for inferring subglacial structures from passive seismic observations (Section 4.4), and we henceforth rely on ice thickness estimates from BedMachine to interpret the observed HVSRs in this study. At other sites where the substation ice thickness estimates have remained consistent between the receiver function studies and BedMachine (Figure 5), the correspondence between f_n^{syn} and f_n^{obs} reinforces the physically meaningful sensitivity of HVSR peak frequencies to subglacial low-velocity zones. Exceptions are noted at KOLR and SIPL, where the significant discrepancies between f_n^{syn} and f_n^{obs} are likely attributed to the limited higher-frequency resolution of receiver functions compared to HVSRs (Section 4.4).

The above findings additionally help to update previous interpretations of Antarctic HVSRs, exemplified using the observed HVSR at ST06 (Figure 6). The unrealistic low-velocity layer in the basal ice proposed by Yan et al. (2018) generates a similar decrease in peak frequency and explains their interpretation, albeit with the limited representation of higher-mode peak energies provided by the DFA model (Text S2 in Supporting Information S1). Carcione et al. (2017) alternatively suggested that the reversed impedance contrast between the ice and subglacial low-velocity zone could entirely explain the f_0^{obs} found at the Whillans Ice Stream (Picotti et al., 2017), supported by BWR forward modeling for an ice layer overlying a variable half-space. However, we find that this instead causes an upwards shift in f_0^{syn} and misidentifies the modes of the observed peaks. The assumption of a subglacial low-velocity zone is therefore required to account correctly for all peaks in the observed HVSRs.

3.3. Seasonal Trends in Observed HVSR Amplitudes

Our inter-annual analysis reveals a clear seasonal trend in observed HVSR amplitudes across all stations within the 0.2–1 Hz frequency range (Figure 7), generally reaching a maximum in the austral late summer and autumn months (February–April) and weakening during the winter and spring. This variability in observed HVSR amplitudes is dependent on the relative coastal proximity of the stations, with weaker and smoother changes in amplitude seen for stations toward the continental interior (e.g., QSPA, ST01, P061; Figure 7) compared to stations closer to the coastline (e.g., ST13, KOLR, DNTW; Figure 7), where observed HVSR amplitudes fluctuate more greatly, over shorter timescales, and across a wider bandwidth. These seasonal trends in observed HVSR amplitudes are also found to be consistent across different years by analyzing stations with multi-year recordings (Figure S22 in Supporting Information S1). In contrast, we find little variability in observed HVSR amplitudes within 0.1–0.2 Hz and no consistent trend across the stations within 0.05–0.1 Hz (Figure 7).

The seasonal trend in observed HVSR amplitudes within 0.2–1 Hz highlights a likely connection to the influence of sea ice cover on short-period secondary ocean microseism energies (Section 1), considering that sea ice coverage over the Southern Ocean is typically minimal in February–April and greatest during August–September (Parkinson & Cavalieri, 2012). We illustrate this connection by computing and comparing relative changes in average observed HVSR amplitudes for each time series between 0.2 and 1 Hz against corresponding 5-day averages of relative sea ice extent in the Southern Ocean (Figure 8). A strong, consistent anti-correlation is mapped between the observed HVSR amplitudes and sea ice extent for all stations, indicating the dominant contribution of secondary microseisms to Antarctic HVSRs within 0.2–1 Hz. We additionally note the clear dependency on the relative coastal proximity of the stations, with both the relative magnitude and volatility of observed HVSR amplitude variability increasing as station distance decreases from the coastline (Figure 8). Our results evidence an enhanced sensitivity of coastal stations to local sea ice conditions compared to interior sites, where higher frequencies are attenuated and recorded energies correlate with longer-wavelength sea ice evolution (Anthony et al., 2015; Grob et al., 2011; Stutzmann et al., 2009).

Figure 5. Comparing synthetic HVSRs against observed HVSRs from 5-day time series during the austral summer at stations with independent constraints on subglacial structure from previous receiver function inversions. The synthetic HVSRs are generated (Text S6 in Supporting Information S1) using the subsurface profiles inferred by Anandakrishnan and Winberry (2004) (dotted red lines) and Chaput et al. (2014) (dashed red lines). SIPL was simultaneously analyzed by both studies, whilst we also include GM01 in reference to Figure 2, where the synthetic HVSR from an ice-basement interface is reasonably assumed considering its location above the Gamburtsev Subglacial Mountains (Figure 2; Aitken et al., 2023). The vertical lines denote the expected f_n from an ice-basement interface up and including $n = 3$ (as described in Figure 3) with ice sheet $V_S = 1{,}900$ m/s and ice thicknesses either fixed from the receiver function studies (blue lines) or assumed from BedMachine (green lines). The associated σ_{f_n} (Section 3.1) are given by the vertical green bars. The solid gray, solid black, dashed black, and dotted black lines are as described in Figures 2b–2d. Refer to Table 1 for the parameters used to generate the synthetic HVSRs and to calculate f_n and σ_{f_n} at each station, and to Figure S21 in Supporting Information S1 for an inter-model comparison including additional stations (Table S3 in Supporting Information S1).

Table 1

Summary of the Subglacial Layers Inferred at the Stations Shown in Figure 5 From the Receiver Function (RF) Inversions of Anandakrishnan and Winberry (2004) (AW2004) and Chaput et al. (2014) (C2014), Alongside the Substation Ice Thicknesses and Uncertainties Used in the RF Studies and Provided by BedMachine

Station	RF study	Subglacial layer inferred by RF study?	Subglacial layer thickness & uncertainty [m]	Subglacial layer V_S [m/s]	Ice thickness & uncertainty [m] (RF study)	Ice thickness & uncertainty [m] (BedMachine)
BYRD	C2014	No	–	–	2,450 ± 90	2,130 ± 30
GM01	Assumed	No	–	–	–	3,110 ± 150
KOLR	C2014	Yes	620 ± 620	610	1,790 ± 300	2,320 ± 30
QSPA*	AW2004	Yes	200 ± 50	850	2,800 ± 30	2,860 ± 40
N052	AW2004	Yes	300 ± 50	~900	2,400 ± 30	2,420 ± 20
SIPL	AW2004; C2014	Yes; Yes	300 ± 50; 200 ± 200	~650; 420	1,020 ± 30; 1,030 ± 150	1,000 ± 30
ST01	C2014	Yes	200 ± 110	450	2,240 ± 300	3,040 ± 30
ST02	C2014	Yes	270 ± 120	610	2,140 ± 90	2,100 ± 110
ST03	No	–	–	C2014	2,230 ± 150	1,920 ± 20
ST04	C2014	Yes	350 ± 120	620	2,960 ± 90	3,090 ± 50
ST06	C2014	Yes	230 ± 100	450	2,400 ± 90	2,680 ± 30
ST08	C2014	Yes	150 ± 100	600	2,300 ± 90	2,320 ± 30
ST09	C2014	Yes	450 ± 600	780	2,140 ± 200	2,740 ± 30
ST10	C2014	Yes	300 ± 120	700	1,130 ± 1,000	1,730 ± 30
ST13	C2014	Yes	250 ± 500	800	1,980 ± 90	2,290 ± 30
ST14	C2014	No	–	–	1,730 ± 90	1,360 ± 40
UPTW	C2014	Yes	350 ± 60	520	2,390 ± 90	2,700 ± 30
WAIS	C2014	No	–	–	3,370 ± 150	3,300 ± 30

Note. *RF inversion performed at old SPA station, ~8 km south of QSPA.

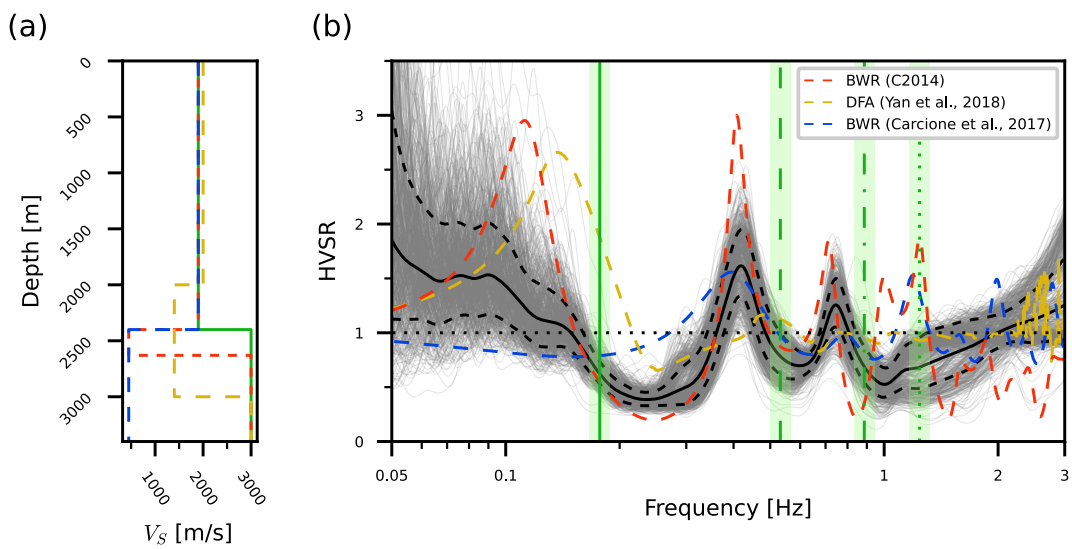

Figure 6. (a) V_S-depth profiles and (b) associated synthetic HVSRs from different assumptions of the Antarctic subsurface, either with the low-velocity subglacial layer inferred from the receiver function inversion of Chaput et al. (2014) (C2014; red dashed line), the low-velocity basal ice layer suggested from the DFA inversion of Yan et al. (2018) (yellow dashed line), or the low-velocity half-space proposed by Carcione et al. (2017) (blue dashed line). The synthetic HVSRs in (b) are compared against the observed HVSR at ST06 (Figure 5). An ice-basement configuration with substation ice thickness from BedMachine is also shown for reference (green solid line in (a)), corresponding to the f_n mapped up to and including $n = 3$ in (b) (green vertical lines), as in Figure 5. The vertical green bars and solid gray, solid black, dashed black, and dotted black lines in (b) are as described in Figures 2b–2d and 5.

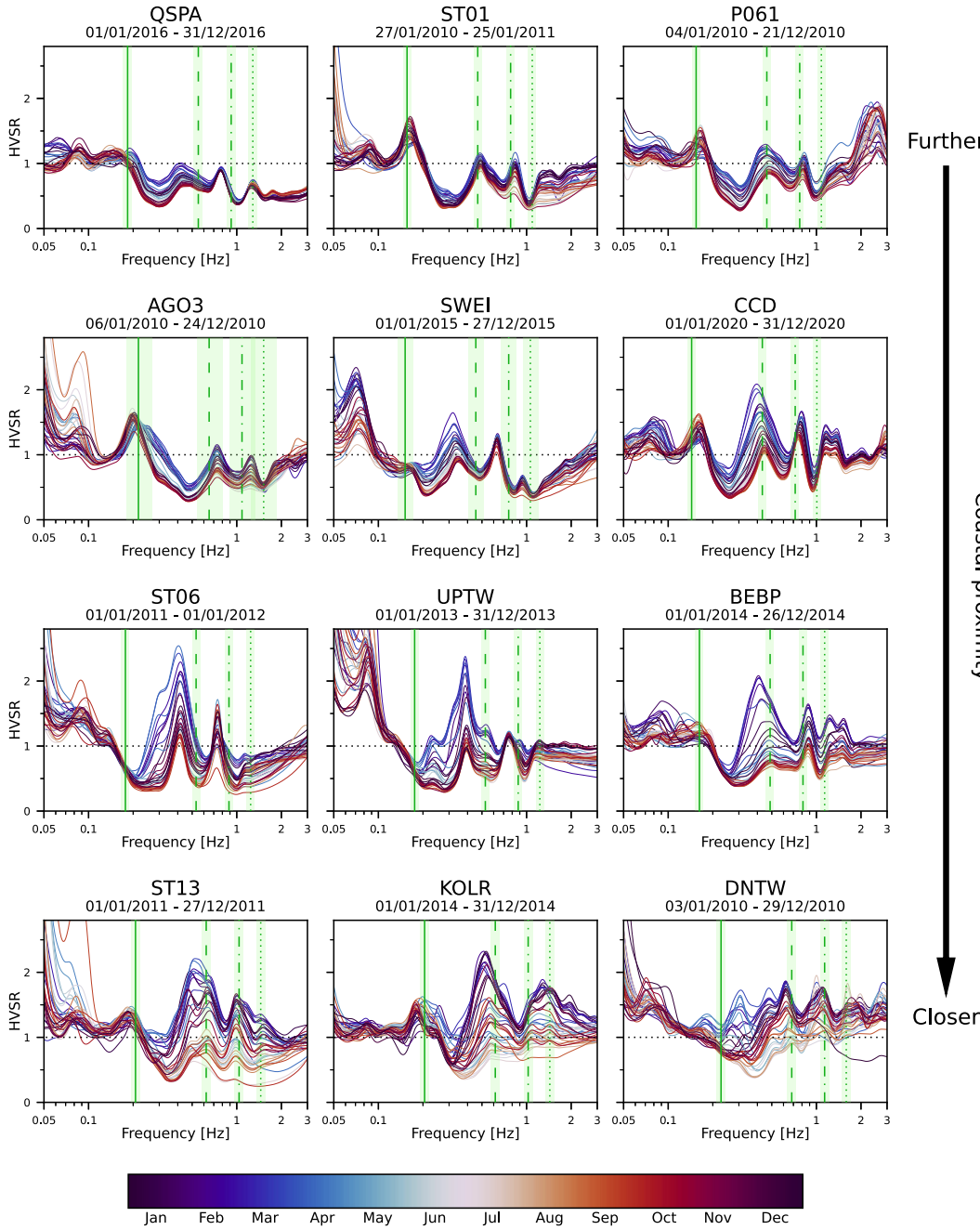

Figure 7. Seasonal trends in observed mean HVSRs for several stations over selected yearly recording periods. Stations are approximately ordered top-down by their relative proximity to the coast (Figure 2), with each HVSR colored according to the central Julian day of the 5-day time series within the yearly period. As in Figure 5, the vertical green lines denote the expected f_n (up to and including $n = 3$) using substation ice thicknesses from BedMachine, with associated uncertainties σ_{f_n} (Section 3.1) given by the vertical green bars. The horizontal black dotted line defines HVSR values of unity.

4. Discussion

4.1. Complexities in Observed HVSRs

Observed HVSRs at several sites exhibit complex behavior and require further interpretation (Text S7 in Supporting Information S1). At some stations (e.g., CCD, AG03; Figure 7), we observe slight evolutions in the frequency of single HVSR peaks with time. This is most clearly discerned at BYRD (Figure 9a), where a rapid

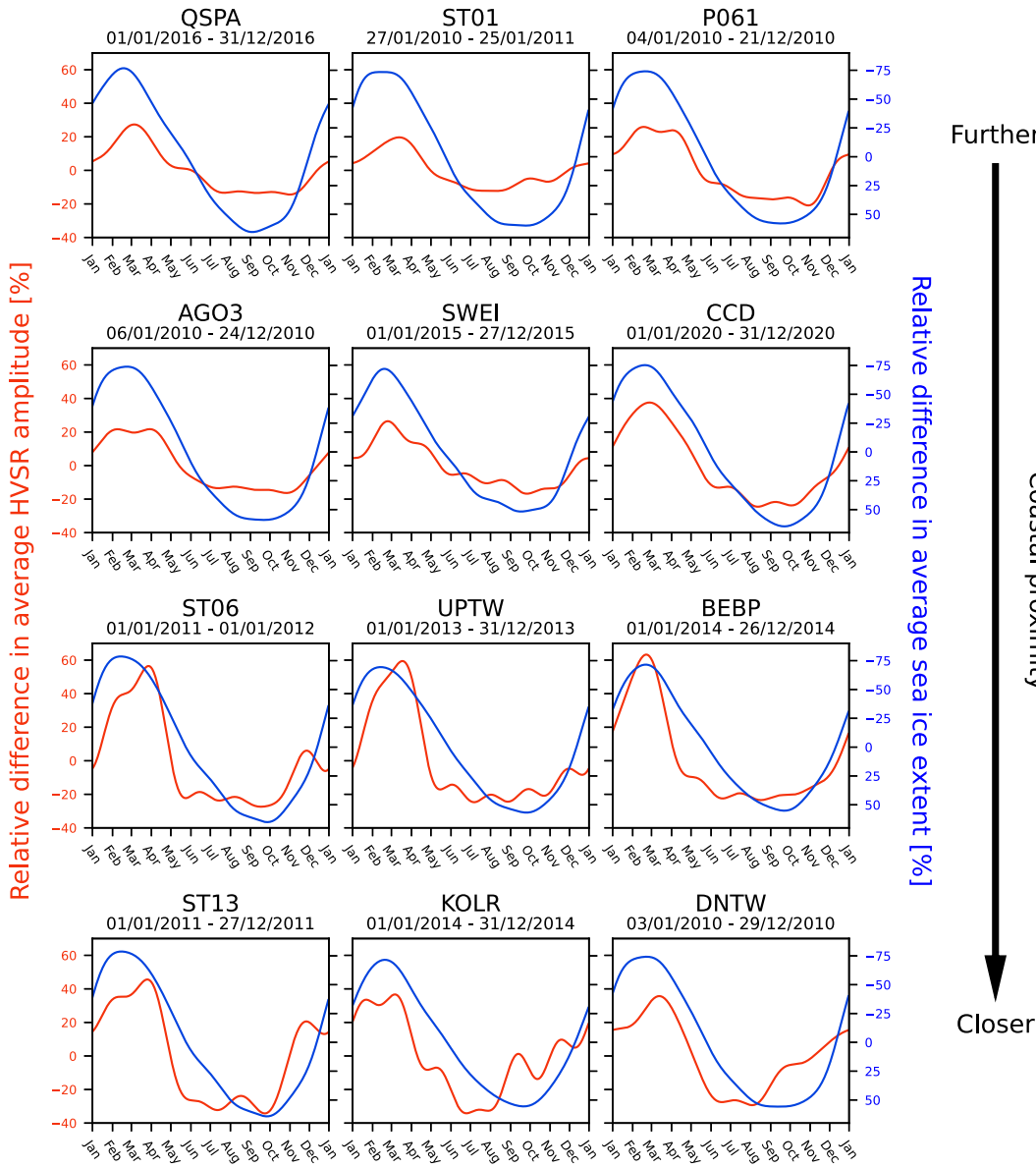

Figure 8. The relative change in mean HVSR amplitudes averaged within 0.2–1 Hz (red lines) against the relative average sea ice extent in the Southern Ocean (blue lines; Fetterer et al., 2017), for each station and yearly period shown in Figure 7. Both variables are averaged within the windows defined by the 5-day HVSR time series and taken relative to the yearly average, with a sixth-order Fourier series fit following Turner et al. (2020). Note the reversal in axis for sea ice extent to highlight the inverse relationship with HVSR amplitudes.

increase in f_0^{obs} from ~0.22 to 0.29 Hz occurs over several days in mid to late January. We attribute this peak frequency behavior to the interaction between non-planar basement topography beneath the station (Figure 9c) and a shift in the dominant propagation direction of the microseism wavefield within ~0.2–0.3 Hz, rather than an implausible change in subsurface conditions (Text S7 in Supporting Information S1). 2-D surface plots of azimuthal HVSR variability (Figure 9b) highlight that the shift in f_0^{obs} occurs with azimuth, initially decreasing below and then jumping above f_0 as the dominant wavefield direction rotates away from north. Notably, this azimuthal pattern in f_0^{obs} inversely correlates with the azimuthal pattern in mean BedMachine ice thickness within the substation footprint (Figure 9d), indicating the presence of non-planar basement topography. We note that the azimuthal variance in mean BedMachine ice thickness (~25 m; Figure 9d) underestimates the shift in f_0^{obs}: this is likely explained by the coarse resolutions (~500 m) and deterministic interpolation schemes used by gridded ice

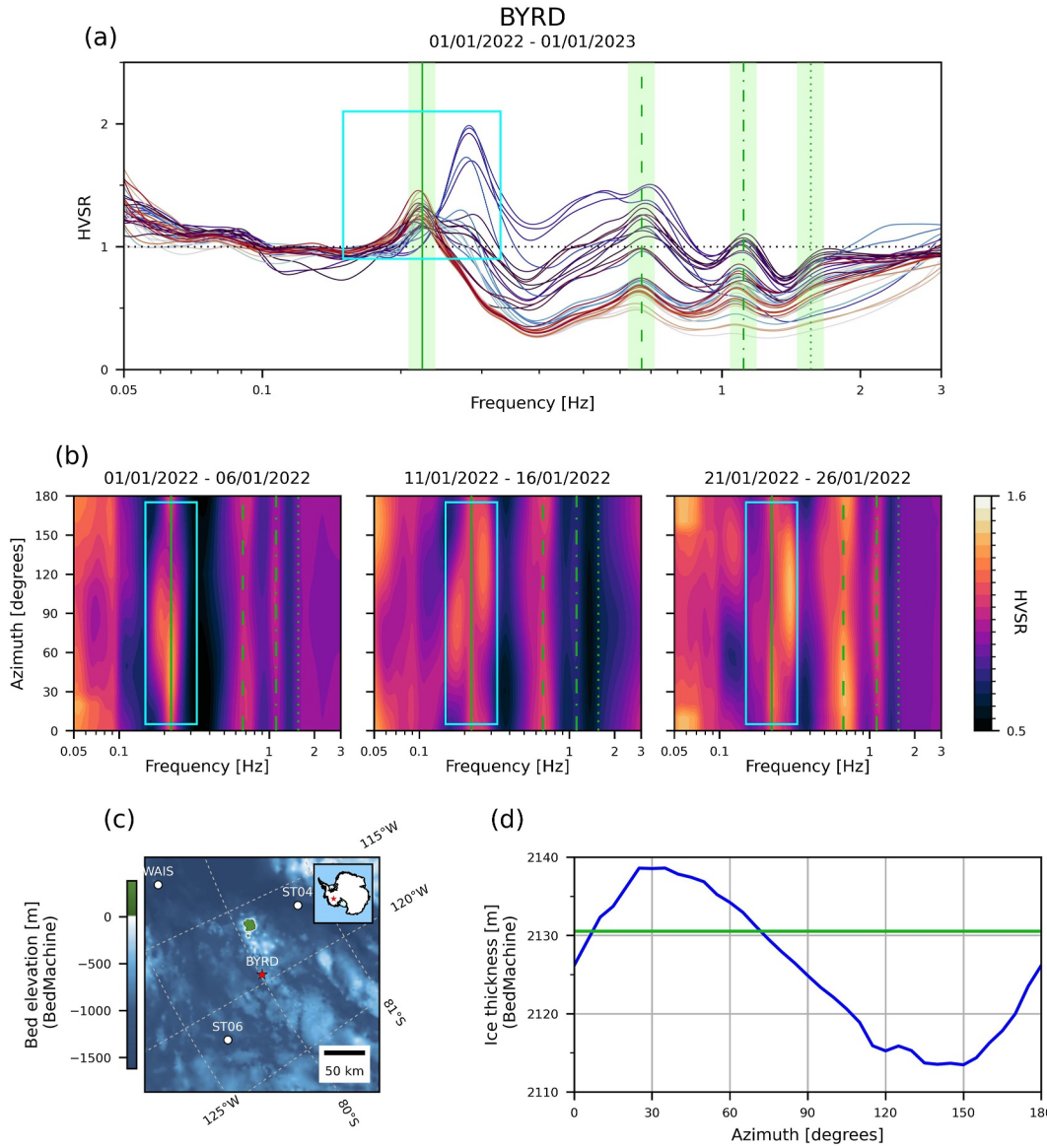

Figure 9. (a) The seasonal trend in observed mean HVSRs at BYRD, with a rapid change in f_0^{obs} in mid to late January (highlighted in cyan box). Other plot details are as described in Figure 7. (b) 2-D surface plots of azimuthal HVSR variability at BYRD, revealing the change in f_0^{obs} to occur with azimuth (highlighted in cyan boxes). As in Figure 5, the vertical green lines denote the expected f_n (up to and including $n = 3$) using the substation ice thickness from BedMachine, assuming a flat ice-basement interface across all azimuths. (c) BedMachine bed elevation around BYRD, illustrating the likelihood of non-planar basement topography beneath the station. (d) The substation ice thickness from BedMachine (green line) compared against the mean BedMachine ice thickness sampled along different azimuths within the substation footprint (blue line), given by a radius equal to the substation ice thickness (Picotti et al., 2017). Note that the azimuth for (b, d) is taken clockwise relative to north.

thickness products such as BedMachine and Bedmap, which fail to capture the true bed relief (e.g., Bartlett et al., 2020; Yin et al., 2022).

Non-planar basement topography can also explain other complexities in our observed HVSRs, including broad and bimodal peaks (e.g., KOLR, ST13; Figure 7) caused by horizontal-component averaging of azimuthally distributed wavefield conditions. We note that our HVSR interpretations are generally limited around the Trans-Antarctic Mountains (Text S7 in Supporting Information S1), where consistently lower f_n^{obs} relative to f_n (e.g., RKST; Figure S23a in Supporting Information S1) are potentially related to steep underlying bed relief

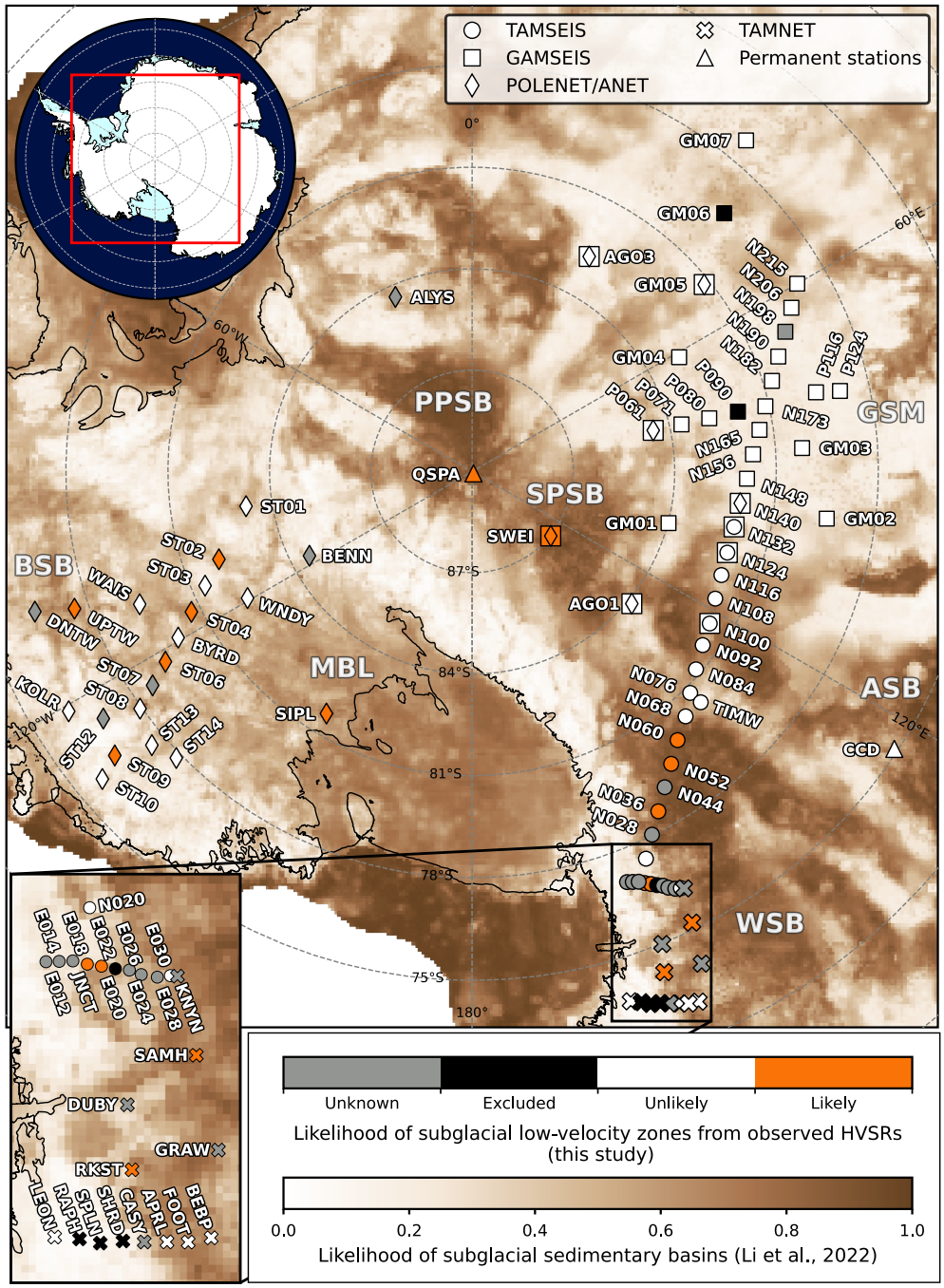

Figure 10. Likelihood of subglacial low-velocity zones inferred from the shift in f_n^{obs} at each station analyzed in this study (color of station markers), compared with the background map of subglacial sedimentary basin likelihood from Li et al. (2022). Stations where we are unable to interpret the observed HVSRs are classified as unknown, whilst stations that lack good-quality data (Text S5 in Supporting Information S1) are excluded from analysis. Station markers and region labels are as per Figure 2.

(Figure S23b in Supporting Information S1) poorly resolved by our observed HVSRs, rather than the presence of a subglacial low-velocity zone. Lower-than-expected f_n^{obs} are found elsewhere, but fall within the high uncertainty range of f_n (e.g., GM03; Figure S23c in Supporting Information S1) due to the lack of RES data coverage and poor resulting constraints on substation ice thickness (Figure S23d in Supporting Information S1). Some stations over the Trans-Antarctic Mountains are additionally affected by transient energies > 1 Hz that distort the observed

HVSRs (e.g., E012; Figure S23e in Supporting Information S1) and likely arise (Text S7 in Supporting Information S1) from wind-forced resonance in nearby outcrops (Figure S23f in Supporting Information S1; Anthony et al., 2015). Meanwhile, a few stations (e.g., DNTW; Figure 7) exhibit highly erratic HVSR behavior without a clear multi-modal resonance pattern (Text S7 in Supporting Information S1): this is possibly caused by a dynamic englacial or subglacial hydrology system, as is inferred beneath DNTW at Thwaites Glacier (Dow, 2022; Hoffman et al., 2020). We additionally note the emergence of weak-amplitude HVSR peaks between ∼0.2–0.3 Hz and ∼0.5–0.6 Hz during the austral summer (e.g., UPTW; Figure 7) that potentially indicate strong englacial layering (Diez et al., 2015) or a stiffer basement capable of inducing secondary peaks from subglacial interfaces (Figure S7d in Supporting Information S1).

4.2. Subglacial Low-Velocity Zones in Antarctica

From our observed HVSRs, we qualitatively infer the likelihood of subglacial low-velocity zones across Antarctica beneath the 82 stations analyzed in this study (Figure 10). For each station, we assess the observed HVSRs across the selected analysis period (Section 2.3) for clear and consistent peaks. The presence of subglacial low-velocity zones is inferred at stations where f_n^{obs} remains below the corresponding lower-bound uncertainty in f_n (i.e., $f_n - \sigma_{f_n}$; Section 3.1) throughout the analysis period and across all azimuths, where f_n and σ_{f_n} use substation ice thicknesses and uncertainties from BedMachine (Section 3.2). The comparison between f_n^{obs} and $f_n - \sigma_{f_n}$ across all azimuths ensures that any possible misinterpretation caused by non-planar basement topography (Section 4.1) is avoided. We avoid interpretations (i.e., unknown likelihood in Figure 10) at stations where a multi-modal resonance pattern from the basement half-space is not clearly discerned (Text S7 in Supporting Information S1).

Our inference (Figure 10) reveals subglacial low-velocity zones with a broad spatial correspondence to major subglacial sedimentary basins (Li et al., 2022), indicating a composition of porous, possibly water saturated sedimentary rocks or overlying deposits of unlithified sediments (Figure 1). Notably, stations in East Antarctica map an expected ice-basement interface across the Gamburtsev Subglacial Mountains, whilst the subglacial packages found beneath N052 and N060 at the southern sub-basin of the Wilkes Subglacial Basin align with gravity and magnetic anomalies interpreting ∼5 km of sedimentary basin fill (Aitken et al., 2023; Frederick et al., 2016). Likewise, the low-velocity zones beneath QSPA and UPTW correlate respectively to the Pensacola-Pole and Byrd subglacial basins (Aitken et al., 2023; Paxman et al., 2019). We note that the general agreement with the map of sedimentary basin likelihood at these sites is unsurprising, given that Li et al. (2022) included the receiver function inversions of Anandakrishnan and Winberry (2004) and Chaput et al. (2014) as training points (Section 3.2).

New and improved insights into the Antarctic IBIZ are yielded from our HVSR analysis. In West Antarctica, the ambiguous presence and distribution of subglacial sedimentary basins (Figure 10) is resolved, with thick subglacial material isolated within the deep troughs of Marie Byrd Land (Figure 2) and away from the elevated highlands around ST10, ST13, and KOLR. Our interpretation at ST09 provides a clear contrast in this region, although could be explained by its location within a subglacial trough (Figure 2) which potentially preserves a local sediment deposit (Aitken et al., 2023). At UPTW, we discover that the subglacial low-velocity zone inferred (Figure 5) coincides with soft lineated bedforms determined by active seismic and radar surveying above the Thwaites Glacier (Holschuh et al., 2020; Muto et al., 2019), providing further context into their formation (Alley et al., 2021). Meanwhile toward the Weddell Coast, the updated ice thickness estimates beneath ST01 (Section 3.2) suggests a continuation in basement rocks between the Ellsworth-Whitmore and Trans-Antarctic Mountains.

In East Antarctica, we highlight the new observation at SWEI, which supports evidence of significant sedimentary fill preserved in the South Pole Subglacial Basin (Aitken et al., 2023). The consistent inference of an ice-basement interface from N068 to the Gamburtsev Subglacial Mountains (Figure 10) aligns with elevated bed topography (Figure 2), indicating that the northward connection between the South Pole and Aurora subglacial basins is more strongly truncated than suggested from Li et al. (2022). An ice-bedrock interface is also identified beneath CCD (Figure 10), which refines existing interpretations from gravity data of the Belgica Subglacial Highlands (Aitken et al., 2023). Along the eastern reaches of the Wilkes Subglacial Basin, a pattern of subglacial low-velocity zones (E018, E020, N036, RKST, SAMH) and ice-bedrock conditions (N028, N020, APRL, FOOT, BEBP) is inferred that conflicts with sedimentary basin likelihoods (Figure 10) and potentially reflects the

complex geological mosaic of the region (Aitken et al., 2023). However, we reiterate that our HVSR interpretations are hindered by the steep bed relief around the Trans-Antarctic Mountains (Text S7 in Supporting Information S1).

4.3. Seasonal Trends in Observed HVSR Amplitudes

In Section 3.3, we identify a clear seasonal trend in observed HVSR amplitudes within 0.2–1 Hz that likely relates to the evolution of sea ice cover in the Southern Ocean and the consequent modulation of short-period secondary microseism energies, consistent with previous studies of single-component seismic noise levels (Section 1).

Ocean microseisms are predominantly associated with Rayleigh waves and vertical particle motion (Gualtieri et al., 2013; Haubrich & McCamy, 1969), which explains the characteristically weak amplitudes of our observed HVSRs (Section 3.2). However, the seasonal trends in HVSR amplitudes (Figure 7) suggest either a relative increase in horizontal-component energies or a relative decrease in vertical-component energies as sea ice retreats. Separating the component spectra (Figure S24 in Supporting Information S1) highlights the dominant variability in horizontal-component energies, but the source of these horizontal-component contributions and reasons behind their seasonal variability are unknown and not investigated further in this study. Possible sources are Love waves in the secondary microseisms (Gualtieri et al., 2020, 2021) or other propagating modes, such as L_g phases (Pratt et al., 2017), Lamb waves guided through the ice sheet (Baker et al., 2019) or body S-waves from the cryoseismic activities of marine-terminating glaciers (Podolskiy & Walter, 2016). Interestingly, we see that the observed HVSR amplitudes are closely aligned in phase with sea ice extent (Figure 8), in contrast to the 20–50-day time lag found for vertical-component spectral amplitudes (Turner et al., 2020). This suggests that the horizontal-component contributions are generated by sources near to the ice sheet margin that are immediately affected by sea ice build-up. The comparative stability of observed HVSR and component spectra amplitudes (Figure 7 and Figure S24 in Supporting Information S1) within the long-period secondary microseism band (0.1–0.2 Hz) also agree with previous findings and suggest distant source locations less affected by sea ice cover, such as from deep ocean storms (Pratt et al., 2017; Turner et al., 2020) or offshore reflections from bathymetric features (Grob et al., 2011). A seasonal modulation of spectral amplitudes in the primary microseism band (0.05–0.1 Hz) is expected as well (Section 1), but is not clearly discerned in our observed HVSRs (Section 3.3), likely due to the impact of low-frequency incoherencies caused by sensor tilt (Text S5 in Supporting Information S1).

4.4. Strengths and Limitations of Using HVSR Peak Frequencies

Our findings establish the capability of HVSRs to determine subglacial low-velocity zones from the shift in f_n^{obs} relative to the f_n expected for the substation ice thickness. This facilitates a straightforward, approximate discrimination of deformable (i.e., subglacial $V_S <$ ice sheet V_S) versus stiff (subglacial $V_S >$ ice sheet V_S) subglacial material, valuable for informing the choice and parameterization of basal sliding/friction laws in ice sheet modeling, which causes substantial variability in projected ice mass loss and sea level rise (e.g., Brondex et al., 2017; Zhao et al., 2025). We demonstrate that the interpretation of HVSR peak frequencies is robust to the seasonal trends in observed HVSR amplitudes, with f_n^{obs} remaining consistent at most stations analyzed in this study (Figure 8). This enables us to infer the presence of subglacial low-velocity zones across Antarctica independent of the recording length or period (Section 4.2). Conversely, we highlight the unreliability in interpreting observed HVSR amplitudes; for instance, seasonal changes in RWE observed over the Greenland Ice Sheet suggested as thermally driven modulations in ice sheet Q_S (Jones et al., 2023) can be additionally or alternatively explained by the seasonal modulation of ocean microseism energies by sea ice cover (Section 3.3). We note that interpretations of HVSR amplitudes are additionally influenced by the choice and parameterization of the forward model (Section 3.1), as well as by deployment factors such as the instrument type and ground-sensor coupling (e.g., Chatelain et al., 2008; Guillier et al., 2008; Molnar et al., 2022).

The key strengths of using HVSR peak frequencies to infer subglacial structure are the short deployment times and wide bandwidths facilitated by seismic ambient noise. Standard guidelines (Molnar et al., 2022) advise minimum window lengths of $10 \times T_m$ s (with $f_m = 1/T_m$ being the lowest frequency considered) and at least 30–60 windows for reliable HVSR interpretations. We conservatively use ambient noise recordings of a few hours for our HVSR investigations over the Antarctic Ice Sheet. aligning with the recommendations of Yan et al. (2018). Nevertheless, this enables subglacial low-velocity zones to be determined from a single day of

fieldwork. The wide bandwidths facilitated by seismic ambient noise are highlighted by comparing the observed HVSRs against the synthetic HVSRs generated using the subglacial layers estimated previously from earthquake receiver functions (Section 3.2). In particular, we highlight the poor fit between the observed and synthetic HVSRs at SIPL (Figure 5), the thinnest ice site considered (Table 1), and the significant uncertainties in subglacial layer thickness estimated by the receiver functions at KOLR (Table 1). The observed HVSRs clearly indicate a considerably thicker or lower-V_S subglacial layer beneath SIPL and exhibit strong peaks at KOLR without any substantial ambiguity (Figure 5). Earthquake receiver functions are limited for shallow crustal investigations (i.e., <1–2 km depth) due to poor signal-to-noise ratios at higher frequencies and ice sheet reverberation multiples complicating arrivals (Anandakrishnan & Winberry, 2004). In contrast, HVSR analyses of seismic ambient noise leverage subsurface resonance and are well suited to studying subglacial structure for most ice sheet and glacier thicknesses (Picotti et al., 2017).

We note that reliable interpretations of subglacial low-velocity zones from HVSR peak frequencies require accurate constraints of substation ice thickness, with the uncertainty in gridded ice thickness estimates being the major contribution to σ_{f_n} (Section 3.1) and hindering our inferences of subglacial low-velocity zone presence across Antarctica (Section 4.2). The use of gridded ice thickness products is particularly limited if non-planar basement topography is significant beneath the station (Section 4.1) and encourages the co-located acquisition of RES or swath radar data (e.g., Holschuh et al., 2020) to map the ice thickness within the substation footprint and fully quantify azimuthal HVSR variability. σ_{f_n} can be further reduced by constraining the ice sheet V_S profile through active seismic measurements. We demonstrate the practical sensitivity of HVSR peak frequencies to the bulk thickness and V_S of subglacial low-velocity zones by using synthetic HVSRs (Figure S25 in Supporting Information S1). Sensitivities to layer thickness and V_S generally decrease with increasing ice thickness; for instance, for a subglacial layer with V_S = 1,000 m/s, the minimum layer thickness reliably detected (assuming an ice thickness uncertainty of 50 m in σ_{f_n}) varies roughly from (55, 65, 105, 135) m with ice thicknesses of (500, 1,000, 2,000, 3,000) m. For typical ice sheet thicknesses (i.e., >500 m), we expect HVSRs to be negligibly sensitive to meter-thick layers of subglacial till (Figure 1), except if the till is extremely low-V_S (i.e., <300 m/s). Sedimentary rock layers with V_S greater than or equal to the ice sheet, meanwhile, primarily affect HVSR amplitudes (e.g., Figure 4) and therefore cannot be reliably detected from HVSRs. Nevertheless, the analysis of HVSR peak frequencies is capable of detecting subglacial layers comprising either a few hundred meters of unlithified sediments or kilometers of sedimentary rocks with V_S less than the overlying ice (Figure S25 in Supporting Information S1). This highlights that the detection and characterization of subglacial sediments using HVSR analysis is a valuable approach to apply over Antarctic sedimentary basins (Section 4.2), which can support significant deposits of both unlithified sediments and sedimentary rocks (Aitken et al., 2023).

4.5. Future Potential of HVSRs

HVSR analyses of seismic ambient noise can promote the rapid and widespread mapping of subglacial low-velocity zones across Antarctica (Section 4.4), particularly over subglacial sedimentary basins where IBIZ structure is poorly known (Section 4.2). High-resolution measurements of substation bed topography (Section 4.4) additionally enable f_n^{obs} to be interpreted separately across different azimuths, potentially inferring the geometry of sedimentary material in subglacial troughs. The deployment of nodal seismic arrays (e.g., Agnew et al., 2025) can leverage relative HVSR amplitudes for refined subsurface interpretations (assuming similar wavefield conditions over the array), including the use of HVSR trough amplitudes, which deepen in response to subglacial low-velocity zones (Guillemot et al., 2024; van Ginkel et al., 2025). Long-term seismic installations, facilitated by step-wise improvements in sensor technology and remote power systems (e.g., Hansen et al., 2015), offer the opportunity to monitor changes in subglacial V_S using HVSRs (Section 1), potentially in real time at telemetered sites. Our findings highlight that changes in subglacial V_S can be reliably distinguished from varying wavefield conditions by shifts in f_n^{obs} that are consistent across all peaks and all azimuths (Section 4.1).

The ability to interpret multiple HVSR peak frequencies reliably suggests a potential framework for robust inversions of subglacial layer thickness and V_S. As supported by Section 3.1, any forward model can be employed to describe HVSR peak frequency behavior (with appropriate consideration of higher SW modes; Text S2 in Supporting Information S1), circumventing ongoing debate regarding the optimal choice of forward model for HVSR inversion (Molnar et al., 2022). The characteristic behavior we find in synthetic HVSR peak frequencies (Section 3.1) moreover highlights a possible basis for HVSR inversions to distinguish subglacial low-velocity

zones associated with unlithified sediments from those associated with sedimentary rocks. For instance, we note the model-independent decrease in f_0^{syn} compared to f_0^{eff} for subglacial layers with extremely low V_S (Section 3.1), likely indicative of fine grained, water saturated sediments (Text S3 in Supporting Information S1). This distinct behavior in HVSR peak frequencies between unlithified sediments and sedimentary rocks is potentially explained by the enhanced trapping of seismic energies in extremely low-velocity layers (Aki & Richards, 2002), causing an increase in the effective resonance path length, as well as attenuation effects that result in HVSR trough deepening (Hobiger et al., 2021). HVSR trough frequencies also exhibit consistent behavior across different models (Figures S8–S15 in Supporting Information S1) and can therefore be incorporated into the inversion framework to provide additional constraints on subsurface structure (Tuan et al., 2011). Future work will aim to develop an inversion framework using HVSR peak and trough frequencies, addressing the ambiguity in qualitative interpretations of f_n^{obs} relative to f_n (Section 4.2) due to the inherent trade-off between subglacial layer thickness and V_S (Figure S25 in Supporting Information S1).

Future HVSR applications offer a valuable complement to other geophysical interpretations of subglacial structure. The combined interpretation of HVSRs and aerogeophysical data can reveal the structure and composition of subglacial sedimentary basins (Section 4.2). Joint inversions with earthquake receiver functions and auto-correlations (e.g., Phạm & Tkalčić, 2018) can leverage the different energies available from the passive seismic wavefield and enhance the capabilities of profiling the Antarctic IBIZ using a single seismic station. The deployment of seismic arrays enables the simultaneous use of microtremor array methods (Hayashi et al., 2022), providing complementary insights into subsurface V_S gradients. Active seismic measurements during sensor deployment or collection can delineate layers of subglacial till (Section 1) and compensate for the limited resolution of HVSR peak frequencies (Section 4.4). Meanwhile, the determination of subglacial conductivity from magnetotellurics (Section 1) has the potential to refine HVSR interpretations of subglacial hydrology (Section 4.1).

4.6. Practical Recommendations

Based on our findings, we provide key recommendations for data collection to guide robust HVSR interpretations of subglacial low-velocity zones in Antarctica (and other ice sheet settings):

- Sensor deployments with strong ground-sensor coupling are preferred (ideally borehole installations in ice) to minimize low-frequency (<0.1 Hz) incoherencies related to sensor tilt (Text S5 in Supporting Information S1) and high-frequency (<1–2 Hz) contamination from wind-driven effects (Text S7 in Supporting Information S1), potentially increasing the number of resolvable resonance modes and depth sensitivity of HVSR interpretations.
- HVSR applications are best suited over subglacial sedimentary basins or other sites with relatively flat basement topography (Section 4.1). Elsewhere, careful analysis of azimuthal HVSR characteristics alongside accurate independent constraints of bed topography within the substation footprint is required to distinguish subglacial low-velocity zones from basement non-planarity. Deploying stations near outcrops or over steep bed relief (e.g., the Trans-Antarctic Mountains) should generally be avoided (Text S7 in Supporting Information S1).
- For short-term deployments, data should ideally be acquired toward the end of the austral summer season (i.e., February–April) to ensure the clearest HVSR peaks for interpretation (Section 3.2). However, longer-term deployments (i.e., ≥1 year) are preferred to assess the influence of varying wavefield conditions (Section 4.1) and provide the potential to monitor changes in subglacial V_S (Section 4.5).

5. Conclusions

In this contribution, we have established that horizontal-to-vertical spectral ratios (HVSRs) of seismic ambient noise can be used to detect subglacial low-velocity zones, owing either to unlithified sediments or porous, water saturated sedimentary rocks, in between the Antarctic Ice Sheet (AIS) and underlying crystalline basement. Through comprehensive 1-D forward modeling of synthetic HVSRs, we identified a decrease in HVSR peak frequencies (compared with the expected peak frequency for an ice-basement interface with no low-velocity zone) that is dependent on the bulk thickness and S-wave velocity (V_S) of the subglacial low-velocity zone, as well as on the overlying ice sheet thickness. This decrease was found to be independent of the forward model and

assumed wavefield composition. Further modeling demonstrated that additional complexity in the Antarctic subsurface (i.e., a surficial firn layer, basal ice variations, sedimentary layering) has a negligible influence on HVSR peak frequency behavior.

We computed and analyzed observed HVSRs for over 80 broadband seismic stations across the AIS. Our observed HVSRs confirmed the physical sensitivity of HVSR peak frequencies to subglacial low-velocity zones and revealed the existence of both fundamental and higher-mode resonance peaks from the V_S contrast defined between the ice (or subglacial material) and the basement. A consistent seasonal trend in observed HVSR amplitudes was also identified within 0.2–1 Hz, which was found to relate to sea ice evolution in the Southern Ocean and the consequent modulation of secondary microseism energies. We additionally highlighted the influence of directional wavefield conditions and non-planar basement topography on the reliable interpretation of HVSR peak frequencies.

Based on our observed HVSR peak frequencies, we inferred the presence of subglacial low-velocity zones across Antarctica, finding a strong spatial correspondence with several known subglacial sedimentary basins. Notably, we refined the presence of thick subglacial material in West Antarctica to subglacial troughs, and confirmed soft bed conditions beneath Thwaites Glacier. In East Antarctica, we provided new constraints on the sedimentary material within the South Pole and Wilkes subglacial basins, and highlighted their delineation by subglacial highlands.

HVSR analysis offers a practical tool to characterize subglacial structure using seismic ambient noise recordings of just a few hours from a single three-component station. The capability for rapid deployments is particularly attractive for improving insights into the remote subglacial sedimentary basins in East Antarctica, where subglacial conditions are poorly known. Short-term deployments should prioritize data acquisition during the late austral summer season to ensure the strongest HVSR peaks. Future HVSR applications have the potential to detect transient variations in subglacial V_S from long-term deployments, with the opportunity to improve understanding of subglacial water drainage and sediment dynamics beneath the AIS. The potential of HVSRs to both improve seismic data coverage across the AIS and facilitate subsurface monitoring at key locations will contribute toward the future understanding of the influence of the ice-bedrock interface zone (IBIZ) on ice sheet behavior.

Conflict of Interest

The authors declare no conflicts of interest relevant to this study.

Availability Statement

The seismic data was retrieved from the Incorporated Research Institutions for Seismology (IRIS) using version 1.4.2 (The ObsPy Development Team, 2025) of the *Obspy* Python package (Beyreuther et al., 2010; Krischer et al., 2015; Megies et al., 2011), with the Federation of Digital Seismograph Networks (FSDN) codes G (for CCD), IU (for QSPA), XP (for the TAMSEIS stations), YT (for the POLENET/ANET stations), ZJ (for the TAMNET stations), and ZM (for the GAMSEIS stations). HVSR data processing was performed using version 1.0.0 (Vantassel, 2021) of the *hvsrpy* Python package (Vantassel, 2025). The forward modeling of synthetic HVSRs was performed using the MATLAB codes available in the Supporting Information S1 of Albarello et al. (2023). The gridded bed topography and ice thickness data sets are provided by Bedmap2 (Fretwell et al., 2022) and version 3 of BedMachine (Morlighem, 2022), whilst the coast and grounding line boundaries plotted in Figures 2 and 10 are provided by MEaSUREs Antarctic Boundaries, version 2 (Mouginot et al., 2017). Daily sea ice extents used for Figure 8 are provided by version 3 of the Sea Ice Index (Fetterer et al., 2017). Figures were made using version 3.10.1 (The Matplotlib Development Team, 2025) of the *Matplotlib* Python package (Hunter, 2007), whilst maps were created using version 0.24.1 (Elson et al., 2024) of the *cartopy* Python package (The Met Office, 2010). High-resolution versions of the manuscript figures and summary plots of HVSR observations from all stations analyzed in this study are archived in Zenodo (Kelly et al., 2025), whilst Python code to download the existing seismic data, compute the observed HVSRs, and reproduce the figures is provided on GitHub (https://github.com/iandalekelly/HVSRs-AntarcticIBIZ).

Acknowledgments
This work was funded through the Australian Research Council (ARC) project DP190100418, with additional support through ARC DP210100834 and the ARC Special Research Initiative, Australian Centre for Excellence in Antarctic Science, SR200100008. I. D. Kelly acknowledges a co-funded Tasmania Graduate Research and Research Training Program Scholarship and the Antarctic Science PhD Scholar Support Grant from the Antarctic Science Foundation. The Scientific Committee on Antarctic Research (SCAR) Instabilities and Thresholds in Antarctica (INSTANT) subcommittee on geothermal heat flow and the Compute Antarctic research group at the University of Tasmania facilitated discussions informing this study. We sincerely thank the editor and Janneke van Ginkel for their helpful suggestions and constructive feedback, which helped us refine and improve this work. Open access publishing facilitated by University of Tasmania, as part of the Wiley - University of Tasmania agreement via the Council of Australasian University Librarians.

References

Agnew, R. S., Pearce, E., Karplus, M., Ranganathan, M., Hoffman, A. O., Hunt, M., et al. (2025). Active and passive seismic surveys over the grounding zone of Eastwind Glacier, Antarctica. *Seismological Research Letters*, *97*(1), 591–605. https://doi.org/10.1785/0220250024

Aitken, A. R. A., Li, L., Kulessa, B., Schroeder, D., Jordan, T. A., Whittaker, J. M., et al. (2023). Antarctic sedimentary basins and their influence on ice-sheet dynamics. *Reviews of Geophysics*, *61*(3), e2021RG000767. https://doi.org/10.1029/2021RG000767

Aitken, A. R. A., Roberts, J. L., van Ommen, T. D., Young, D. A., Golledge, N. R., Greenbaum, J. S., et al. (2016). Repeated large-scale retreat and advance of Totten Glacier indicated by inland bed erosion. *Nature*, *533*(7603), 385–389. https://doi.org/10.1038/nature17447

Aitken, A. R. A., Young, D. A., Ferraccioli, F., Betts, P. G., Greenbaum, J. S., Richter, T. G., et al. (2014). The subglacial geology of Wilkes Land, East Antarctica. *Geophysical Research Letters*, *41*(7), 2390–2400. https://doi.org/10.1002/2014GL059405

Aki, K., & Richards, P. G. (2002). *Quantitative seismology*. University Science Books.

Albarello, D., Herak, M., Lunedei, E., Paolucci, E., & Tanzini, A. (2023). Simulating H/V spectral ratios (HVSR) of ambient vibrations: A comparison among numerical models. *Geophysical Journal International*, *234*(2), 870–878. https://doi.org/10.1093/gji/ggad109

Alley, R. B., Holschuh, N., MacAyeal, D. R., Parizek, B. R., Zoet, L., Riverman, K., et al. (2021). Bedforms of Thwaites Glacier, West Antarctica: Character and origin. *Journal of Geophysical Research, Earth Surface*, *126*(12), e2021JF006339. https://doi.org/10.1029/2021JF006339

Anandakrishnan, S., & Winberry, J. P. (2004). Antarctic subglacial sedimentary layer thickness from receiver function analysis. *Global and Planetary Change*, *42*(1), 167–176. https://doi.org/10.1016/j.gloplacha.2003.10.005

Anthony, R. E., Aster, R. C., & McGrath, D. (2017). Links between atmosphere, ocean, and cryosphere from two decades of microseism observations on the Antarctic Peninsula. *Journal of Geophysical Research, Earth Surface*, *122*(1), 153–166. https://doi.org/10.1002/2016JF004098

Anthony, R. E., Aster, R. C., Wiens, D., Nyblade, A., Anandakrishnan, S., Huerta, A., et al. (2015). The seismic noise environment of Antarctica. *Seismological Research Letters*, *86*(1), 89–100. https://doi.org/10.1785/0220140109

Anthony, R. E., Ringler, A. T., DuVernois, M., Anderson, K. R., & Wilson, D. C. (2021). Six decades of seismology at South Pole, Antarctica: Current limitations and future opportunities to facilitate new geophysical observations. *Seismological Research Letters*, *92*(5), 2718–2735. https://doi.org/10.1785/0220200448

Ardhuin, F., Stutzmann, E., Schimmel, M., & Mangeney, A. (2011). Ocean wave sources of seismic noise. *Journal of Geophysical Research: Oceans*, *116*(C9), C09004. https://doi.org/10.1029/2011JC006952

Ashmore, D. W., & Bingham, R. G. (2014). Antarctic subglacial hydrology: Current knowledge and future challenges. *Antarctic Science*, *26*(6), 758–773. https://doi.org/10.1017/S0954102014000546

Baker, M. G., Aster, R. C., Anthony, R. E., Chaput, J., Wiens, D. A., Nyblade, A., et al. (2019). Seasonal and spatial variations in the ocean-coupled ambient wavefield of the Ross ice shelf. *Journal of Glaciology*, *65*(254), 912–925. https://doi.org/10.1017/jog.2019.64

Bard, P.-Y. (1999). Microtremor measurements: A tool for site effect estimation. In *Proceedings the effects of surface geology on seismic motion* (Vol. 3, pp. 1251–1279).

Bartlett, O. T., Palmer, S. J., Schroeder, D. M., MacKie, E. J., Barrows, T. T., & Graham, A. G. C. (2020). Geospatial simulations of airborne ice-penetrating radar surveying reveal elevation under-measurement bias for ice-sheet bed topography. *Annals of Glaciology*, *61*(81), 46–57. https://doi.org/10.1017/aog.2020.35

Benkaci, N., Oubaiche, E. H., Chatelain, J.-L., Bensalem, R., Benouar, D., & Abbes, K. (2021). Non-stability and non-reproducibility of ambient vibration HVSR peaks in Algiers (Algeria). *Journal of Earthquake Engineering*, *25*(5), 853–871. https://doi.org/10.1080/13632469.2018.1537903

Bès de Berc, M., Zigone, D., Danecek, P., Steyer, A., Zanolin, F., Maggi, A., et al. (2023). A new posthole seismometer at Concordia permanent research facility in the heart of the icy East Antarctic plateau. *Seismological Research Letters*, *95*(3), 1518–1532. https://doi.org/10.1785/0220230188

Beyreuther, M., Barsch, R., Krischer, L., Megies, T., Behr, Y., & Wassermann, J. (2010). ObsPy: A Python toolbox for seismology. *Seismological Research Letters*, *81*(3), 530–533. https://doi.org/10.1785/gssrl.81.3.530

Bonnefoy-Claudet, S., Cornou, C., Bard, P.-Y., Cotton, F., Moczo, P., Kristek, J., & Fäh, D. (2006). H/V ratio: A tool for site effects evaluation. Results from 1-D noise simulations. *Geophysical Journal International*, *167*(2), 827–837. https://doi.org/10.1111/j.1365-246X.2006.03154.x

Bonnefoy-Claudet, S., Cotton, F., & Bard, P. (2006). The nature of noise wavefield and its applications for site effects studies: A literature review. *Earth-Science Reviews*, *79*(3–4), 205–227. https://doi.org/10.1016/j.earscirev.2006.07.004

Brisbourne, A. M., Smith, A. M., Vaughan, D. G., King, E. C., Davies, D., Bingham, R. G., et al. (2017). Bed conditions of Pine Island Glacier, West Antarctica. *Journal of Geophysical Research, Earth Surface*, *122*(1), 419–433. https://doi.org/10.1002/2016jf004033

Brondex, J., Gagliardini, O., Gillet-Chaulet, F., & Durand, G. (2017). Sensitivity of grounding line dynamics to the choice of the friction law. *Journal of Glaciology*, *63*(241), 854–866. https://doi.org/10.1017/jog.2017.51

Cairns, G. J., Benham, G. P., & Hewitt, I. J. (2025). Groundwater dynamics beneath a marine ice sheet. *The Cryosphere*, *19*(9), 3725–3747. https://doi.org/10.5194/tc-19-3725-2025

Carcione, J. M., Picotti, S., Francese, R., Giorgi, M., & Pettenati, F. (2017). Effect of soil and bedrock anelasticity on the S-wave amplification function. *Geophysical Journal International*, *208*(1), 424–431. https://doi.org/10.1093/gji/ggw402

Chaput, J., Aster, R. C., Huerta, A., Sun, X., Lloyd, A., Wiens, D., et al. (2014). The crustal thickness of West Antarctica. *Journal of Geophysical Research: Solid Earth*, *119*(1), 378–395. https://doi.org/10.1002/2013JB010642

Chatelain, J.-L., Guillier, B., Cara, F., Duval, A.-M., Atakan, K., Bard, P.-Y., & The WP02 SESAME team. (2008). Evaluation of the influence of experimental conditions on H/V results from ambient noise recordings. *Bulletin of Earthquake Engineering*, *6*(1), 33–74. https://doi.org/10.1007/s10518-007-9040-7

Cheng, T., Cox, B. R., Vantassel, J. P., & Manuel, L. (2020). A statistical approach to account for azimuthal variability in single-station HVSR measurements. *Geophysical Journal International*, *223*(2), 1040–1053. https://doi.org/10.1093/gji/ggaa342

Constable, A. J., Harper, S., Dawson, J., Holsman, K., Mustonen, T., Piepenburg, D., et al. (2022). Cross-chapter paper 6: Polar regions. In *Climate change 2022: Impacts, adaptation and vulnerability* (pp. 2319–2368). University Press.

Cox, B. R., Cheng, T., Vantassel, J. P., & Manuel, L. (2020). A statistical representation and frequency-domain window-rejection algorithm for single-station HVSR measurements. *Geophysical Journal International*, *221*(3), 2170–2183. https://doi.org/10.1093/gji/ggaa119

Dawson, E. J., Schroeder, D. M., Chu, W., Mantelli, E., & Seroussi, H. (2022). Ice mass loss sensitivity to the Antarctic ice sheet basal thermal state. *Nature Communications*, *13*(1), 4957. https://doi.org/10.1038/s41467-022-32632-2

Dawson, E. J., Schroeder, D. M., Chu, W., Mantelli, E., & Seroussi, H. (2024). Heterogeneous basal thermal conditions underpinning the Adélie-George V Coast, East Antarctica. *Geophysical Research Letters*, *51*(2), e2023GL105450. https://doi.org/10.1029/2023GL105450

Diez, A., & Eisen, O. (2015). Seismic wave propagation in anisotropic ice – Part 1: Elasticity tensor and derived quantities from ice-core properties. *The Cryosphere*, *9*(1), 367–384. https://doi.org/10.5194/tc-9-367-2015

Diez, A., Eisen, O., Hofstede, C., Lambrecht, A., Mayer, C., Miller, H., et al. (2015). Seismic wave propagation in anisotropic ice – Part 2: Effects of crystal anisotropy in geophysical data. *The Cryosphere*, *9*(1), 385–398. https://doi.org/10.5194/tc-9-385-2015

Dou, S., & Ajo-Franklin, J. B. (2014). Full-wavefield inversion of surface waves for mapping embedded low-velocity zones in permafrost. *Geophysics*, *79*(6), EN107–EN124. https://doi.org/10.1190/geo2013-0427.1

Dow, C. F. (2022). The role of subglacial hydrology in Antarctic ice sheet dynamics and stability: A modelling perspective. *Annals of Glaciology*, *63*(87–89), 49–54. https://doi.org/10.1017/aog.2023.9

Dunham, C. K., O'Donnell, J. P., Stuart, G. W., Brisbourne, A. M., Rost, S., Jordan, T. A., et al. (2020). A joint inversion of receiver function and Rayleigh wave phase velocity dispersion data to estimate crustal structure in West Antarctica. *Geophysical Journal International*, *223*(3), 1644–1657. https://doi.org/10.1093/gji/ggaa398

Elson, P., de Andrade, E. S., Lucas, G., May, R., Hattersley, R., Campbell, E., et al. (2024). SciTools/cartopy: October 8, 2024 release (version 0.24.1) [Software]. *Zenodo*. https://doi.org/10.5281/zenodo.13905945

Evans, D., Phillips, E., Hiemstra, J., & Auton, C. (2006). Subglacial till: Formation, sedimentary characteristics and classification. *Earth-Science Reviews*, *78*(1–2), 115–176. https://doi.org/10.1016/j.earscirev.2006.04.001

Fäh, D., Kind, F., & Giardini, D. (2001). A theoretical investigation of average H/V ratios. *Geophysical Journal International*, *145*(2), 535–549. https://doi.org/10.1046/j.0956-540x.2001.01406.x

Farazi, A. H., Hossain, M. S., Ito, Y., Piña-Flores, J., Kamal, A. S. M. M., & Rahman, M. Z. (2023). Shear wave velocity estimation in the Bengal Basin, Bangladesh by HVSR analysis: Implications for engineering bedrock depth. *Journal of Applied Geophysics*, *211*, 104967. https://doi.org/10.1016/j.jappgeo.2023.104967

Fetterer, F., Knowles, K., Meier, W., & Savoie, M. (2017). Sea ice index (version 3) [Dataset]. *NASA National Snow and Ice Data Center Distributed Active Archive Center*. https://doi.org/10.7265/N5K072F8

Field, E., & Jacob, K. (1993). The theoretical response of sedimentary layers to ambient seismic noise. *Geophysical Research Letters*, *20*(24), 2925–2928. https://doi.org/10.1029/93GL03054

Foti, S., Hollender, F., Garofalo, F., Albarello, D., Asten, M., Bard, P.-Y., et al. (2018). Guidelines for the good practice of surface wave analysis: A product of the InterPACIFIC project. *Bulletin of Earthquake Engineering*, *16*(6), 2367–2420. https://doi.org/10.1007/s10518-017-0206-7

Franke, S., Gerber, T., Warren, C., Jansen, D., Eisen, O., & Dahl-Jensen, D. (2023). Investigating the radar response of englacial debris entrained basal ice units in East Antarctica using electromagnetic forward modeling. *IEEE Transactions on Geoscience and Remote Sensing*, *61*, 1–16. https://doi.org/10.1109/TGRS.2023.3277874

Frederick, B. C., Young, D. A., Blankenship, D. D., Richter, T. G., Kempf, S. D., Ferraccioli, F., & Siegert, M. J. (2016). Distribution of subglacial sediments across the Wilkes subglacial basin, East Antarctica. *Journal of Geophysical Research, Earth Surface*, *121*(4), 790–813. https://doi.org/10.1002/2015JF003760

Fretwell, P., Pritchard, H. D., Vaughan, D. G., Bamber, J. L., Barrand, N. E., Bell, R., et al. (2013). Bedmap2: Improved ice bed, surface and thickness datasets for Antarctica. *The Cryosphere*, *7*(1), 375–393. https://doi.org/10.5194/tc-7-375-2013

Fretwell, P., Pritchard, H. D., Vaughan, D. G., Bamber, J. L., Barrand, N. E., Bell, R., et al. (2022). BEDMAP2—Ice thickness, bed and surface elevation for Antarctica—Gridding products (version 1) [Dataset]. *NERC EDS UK Polar Data Centre*. https://doi.org/10.5285/fa5d606c-dc95-47ee-9016-7a82e446f2f2

Fricker, H. A., Galton-Fenzi, B. K., Walker, C. C., Freer, B. I. D., Padman, L., & DeConto, R. (2025). Antarctica in 2025: Drivers of deep uncertainty in projected ice loss. *Science*, *387*(6734), 601–609. https://doi.org/10.1126/science.adt9619

Fu, L., Guo, J., Li, L., Lu, K., & Chen, X. (2023). A local seismic project near the Dalk Glacier area, Larsemann Hills, East Antarctica: Toward Subice imaging and icequake monitoring. *Seismological Research Letters*, *94*(4), 2083–2092. https://doi.org/10.1785/0220220372

Fyke, J., Sergienko, O., Löfverström, M., Price, S., & Lenaerts, J. T. M. (2018). An overview of interactions and feedbacks between ice sheets and the Earth system. *Reviews of Geophysics*, *56*(2), 361–408. https://doi.org/10.1029/2018RG000600

García-Jerez, A., Luzón, F., Navarro, M., & Pérez-Ruiz, J. A. (2006). Characterization of the sedimentary cover of the Zafarraya Basin, southern Spain, by means of ambient noise. *Bulletin of the Seismological Society of America*, *96*(3), 957–967. https://doi.org/10.1785/0120050061

Gong, D., Fan, X., Li, Y., Li, B., Zhang, N., Gromig, R., et al. (2019). Coring of Antarctic subglacial sediments. *Journal of Marine Science and Engineering*, *7*(6), 194. https://doi.org/10.3390/jmse7060194

Goodge, J. W., Severinghaus, J. P., Johnson, J., Tosi, D., & Bay, R. (2021). Deep ice drilling, bedrock coring and dust logging with the rapid access ice drill (RAID) at Minna Bluff, Antarctica. *Annals of Glaciology*, *62*(85–86), 324–339. https://doi.org/10.1017/aog.2021.13

Grob, M., Maggi, A., & Stutzmann, E. (2011). Observations of the seasonality of the Antarctic microseismic signal, and its association to sea ice variability. *Geophysical Research Letters*, *38*(11), L11302. https://doi.org/10.1029/2011GL047525

Gualtieri, L., Bachmann, E., Simons, F. J., & Tromp, J. (2020). The origin of secondary microseism love waves. *Proceedings of the National Academy of Sciences*, *117*(47), 29504–29511. https://doi.org/10.1073/pnas.2013806117

Gualtieri, L., Bachmann, E., Simons, F. J., & Tromp, J. (2021). Generation of secondary microseism love waves: Effects of bathymetry, 3-D structure and source seasonality. *Geophysical Journal International*, *226*(1), 192–219. https://doi.org/10.1093/gji/ggab095

Gualtieri, L., Stutzmann, E., Capdeville, Y., Ardhuin, F., Schimmel, M., Mangeney, A., & Morelli, A. (2013). Modelling secondary microseismic noise by normal mode summation. *Geophysical Journal International*, *193*(3), 1732–1745. https://doi.org/10.1093/gji/ggt090

Gualtieri, L., Stutzmann, E., Juretzek, C., Hadziioannou, C., & Ardhuin, F. (2019). Global scale analysis and modelling of primary microseisms. *Geophysical Journal International*, *218*(1), 560–572. https://doi.org/10.1093/gji/ggz161

Guillemot, A., Bontemps, N., Larose, E., Teodor, D., Faller, S., Baillet, L., et al. (2024). Investigating subglacial water-filled cavities by spectral analysis of ambient seismic noise: Results on the polythermal Tête-Rousse Glacier (Mont Blanc, France). *Geophysical Research Letters*, *51*(4), e2023GL105038. https://doi.org/10.1029/2023GL105038

Guillier, B., Atakan, K., Chatelain, J.-L., Havskov, J., Ohrnberger, M., Cara, F., et al. (2008). Influence of instruments on the H/V spectral ratios of ambient vibrations. *Bulletin of Earthquake Engineering*, *6*(1), 3–31. https://doi.org/10.1007/s10518-007-9039-0

Guillier, B., Chatelain, J.-L., Bonnefoy-Claudet, S., & Haghshenas, E. (2007). Use of ambient noise: From spectral amplitude variability to H/V stability. *Journal of Earthquake Engineering*, *11*(6), 925–942. https://doi.org/10.1080/13632460701457249

Gustafson, C. D., Key, K., Siegfried, M. R., Winberry, J. P., Fricker, H. A., Venturelli, R. A., & Michaud, A. B. (2022). A dynamic saline groundwater system mapped beneath an Antarctic ice stream. *Science*, *376*(6593), 640–644. https://doi.org/10.1126/science.abm3301

Haghshenas, E., Bard, P.-Y., & Theodulidis, N. (2008). Empirical evaluation of microtremor H/V spectral ratio. *Bulletin of Earthquake Engineering*, *6*(1), 75–108. https://doi.org/10.1007/s10518-007-9058-x

Hansen, S. E., Nyblade, A. A., Heeszel, D. S., Wiens, D. A., Shore, P., & Kanao, M. (2010). Crustal structure of the Gamburtsev Mountains, East Antarctica, from S-wave receiver functions and Rayleigh wave phase velocities. *Earth and Planetary Science Letters*, *300*(3), 395–401. https://doi.org/10.1016/j.epsl.2010.10.022

Hansen, S. E., Reusch, A. M., Parker, T., Bloomquist, D. K., Carpenter, P., Graw, J. H., & Brenn, G. R. (2015). The transantarctic mountains northern network (TAMNET): Deployment and performance of a seismic array in Antarctica. *Seismological Research Letters*, *86*(6), 1636–1644. https://doi.org/10.1785/0220150117

Hasselmann, K. (1963). A statistical analysis of the generation of microseisms. *Reviews of Geophysics*, *1*(2), 177–210. https://doi.org/10.1029/RG001i002p00177

Haubrich, R. A., & McCamy, K. (1969). Microseisms: Coastal and pelagic sources. *Reviews of Geophysics*, *7*(3), 539–571. https://doi.org/10.1029/RG007i003p00539

Hayashi, K., Asten, M. W., Stephenson, W. J., Cornou, C., Hobiger, M., Pilz, M., & Yamanaka, H. (2022). Microtremor array method using spatial autocorrelation analysis of Rayleigh-wave data. *Journal of Seismology*, *26*(4), 601–627. https://doi.org/10.1007/s10950-021-10051-y

Hobiger, M., Hallo, M., Schmelzbach, C., Stähler, S. C., Fäh, D., Giardini, D., et al. (2021). The shallow structure of Mars at the InSight landing site from inversion of ambient vibrations. *Nature Communications*, *12*(1), 6756. https://doi.org/10.1038/s41467-021-26957-7

Hoffman, A. O., Christianson, K., Shapero, D., Smith, B. E., & Joughin, I. (2020). Brief communication: Heterogenous thinning and subglacial lake activity on Thwaites Glacier, West Antarctica. *The Cryosphere*, *14*(12), 4603–4609. https://doi.org/10.5194/tc-14-4603-2020

Holschuh, N., Christianson, K., Paden, J., Alley, R., & Anandakrishnan, S. (2020). Linking postglacial landscapes to glacier dynamics using swath radar at Thwaites Glacier, Antarctica. *Geology*, *48*(3), 268–272. https://doi.org/10.1130/G46772.1

Horgan, H. J., Anandakrishnan, S., Alley, R. B., Burkett, P. G., & Peters, L. E. (2011). Englacial seismic reflectivity: Imaging crystal-orientation fabric in West Antarctica. *Journal of Glaciology*, *57*(204), 639–650. https://doi.org/10.3189/002214311797409686

Hunter, J. D. (2007). Matplotlib: A 2D graphics environment. *Computing in Science & Engineering*, *9*(3), 90–95. https://doi.org/10.1109/MCSE.2007.55

Ibs-von Seht, M., & Wohlenberg, J. (1999). Microtremor measurements used to map thickness of soft sediments. *Bulletin of the Seismological Society of America*, *89*(1), 250–259. https://doi.org/10.1785/BSSA0890010250

Jones, G. A., Ferreira, A. M. G., Kulessa, B., Schimmel, M., Berbellini, A., & Morelli, A. (2023). Constraints on the cryohydrological warming of Firn and ice in Greenland from Rayleigh wave ellipticity data. *Geophysical Research Letters*, *50*(15), e2023GL103673. https://doi.org/10.1029/2023GL103673

Jordan, T. A., Thompson, S., Kulessa, B., & Ferraccioli, F. (2023). Geological sketch map and implications for ice flow of Thwaites Glacier, West Antarctica, from integrated aerogeophysical observations. *Science Advances*, *9*(22), eadf2639. https://doi.org/10.1126/sciadv.adf2639

Kawase, H., Matsushima, S., Satoh, T., & Sánchez-Sesma, F. J. (2015). Applicability of theoretical horizontal-to-vertical ratio of microtremors based on the diffuse field concept to previously observed data. *Bulletin of the Seismological Society of America*, *105*(6), 3092–3103. https://doi.org/10.1785/0120150134

Kawase, H., Mori, Y., & Nagashima, F. (2018). Difference of horizontal-to-vertical spectral ratios of observed earthquakes and microtremors and its application to S-wave velocity inversion based on the diffuse field concept. *Earth Planets and Space*, *70*(1), 1. https://doi.org/10.1186/s40623-017-0766-4

Kelly, I. D., Reading, A. M., Stål, T., Kulessa, B., García-Jerez, A., Piña-Flores, J., et al. (2025). Determining the character of subglacial sediments in the ice-bedrock interface zone of Antarctica using horizontal-to-vertical spectral ratios (HVSRs) of seismic ambient noise (version 1.0.0) [Dataset]. *Zenodo*. https://doi.org/10.5281/zenodo.15762976

Koellner, S., Parizek, B. R., Alley, R. B., Muto, A., & Holschuh, N. (2019). The impact of spatially-variable basal properties on outlet glacier flow. *Earth and Planetary Science Letters*, *515*, 200–208. https://doi.org/10.1016/j.epsl.2019.03.026

Köhler, A., Maupin, V., Nuth, C., & van Pelt, W. (2019). Characterization of seasonal glacial seismicity from a single-station on-ice record at Holtedahlfonna, Svalbard. *Annals of Glaciology*, *60*(79), 23–36. https://doi.org/10.1017/aog.2019.15

Köhler, A., & Weidle, C. (2019). Potentials and pitfalls of permafrost active layer monitoring using the HVSR method: A case study in Svalbard. *Earth Surface Dynamics*, *7*(1), 1–16. https://doi.org/10.5194/esurf-7-1-2019

Konno, K., & Ohmachi, T. (1998). Ground-motion characteristics estimated from spectral ratio between horizontal and vertical components of microtremor. *Bulletin of the Seismological Society of America*, *88*(1), 228–241. https://doi.org/10.1785/BSSA0880010228

Krischer, L., Megies, T., Barsch, R., Beyreuther, M., Lecocq, T., Caudron, C., & Wassermann, J. (2015). ObsPy: A bridge for seismology into the scientific python ecosystem. *Computational Science & Discovery*, *8*(1), 014003. https://doi.org/10.1088/1749-4699/8/1/014003

Kuhl, T., Gibson, C., Johnson, J., Boeckmann, G., Moravec, E., & Slawny, K. (2021). Agile sub-ice geological (ASIG) drill development and Pirrit Hills field project. *Annals of Glaciology*, *62*(84), 53–66. https://doi.org/10.1017/aog.2020.59

Kula, D., Olszewska, D., Dobiński, W., & Glazer, M. (2018). Horizontal-to-vertical spectral ratio variability in the presence of permafrost. *Geophysical Journal International*, *214*(1), 219–231. https://doi.org/10.1093/gji/ggy118

Kulessa, B., Hubbard, A. L., Booth, A. D., Bougamont, M., Dow, C. F., Doyle, S. H., et al. (2017). Seismic evidence for complex sedimentary control of Greenland ice sheet flow. *Science Advances*, *3*(8), e1603071. https://doi.org/10.1126/sciadv.1603071

Lachet, C., & Bard, P.-Y. (1994). Numerical and theoretical investigations on the possibilities and limitations of Nakamura's technique. *Journal of Physics of the Earth*, *42*(5), 377–397. https://doi.org/10.4294/jpe1952.42.377

Langston, C. A. (1977). The effect of planar dipping structure on source and receiver responses for constant ray parameter. *Bulletin of the Seismological Society of America*, *67*(4), 1029–1050. https://doi.org/10.1785/BSSA0670041029

Lawrence, J. F., Wiens, D. A., Nyblade, A. A., Anandakrishnan, S., Shore, P. J., & Voigt, D. (2006). Rayleigh wave phase velocity analysis of the Ross Sea, Transantarctic Mountains, and East Antarctica from a temporary seismograph array. *Journal of Geophysical Research*, *111*(B6), B06302. https://doi.org/10.1029/2005JB003812

Lévêque, J.-J., Maggi, A., & Souriau, A. (2010). Seismological constraints on ice properties at Dome C, Antarctica, from horizontal to vertical spectral ratios. *Antarctic Science*, *22*(5), 572–579. https://doi.org/10.1017/S0954102010000325

Li, L., Aitken, A. R. A., Lindsay, M. D., & Kulessa, B. (2022). Sedimentary basins reduce stability of Antarctic ice streams through groundwater feedbacks. *Nature Geoscience*, *15*(8), 645–650. https://doi.org/10.1038/s41561-022-00992-5

Livingstone, S. J., Li, Y., Rutishauser, A., Sanderson, R. J., Winter, K., Mikucki, J. A., et al. (2022). Subglacial lakes and their changing role in a warming climate. *Nature Reviews Earth & Environment*, *3*(2), 106–124. https://doi.org/10.1038/s43017-021-00246-9

Llorens, M., Griera, A., Bons, P. D., Gomez-Rivas, E., Weikusat, I., Prior, D. J., et al. (2020). Seismic anisotropy of temperate ice in polar ice sheets. *Journal of Geophysical Research, Earth Surface*, *125*(11), e2020JF005714. https://doi.org/10.1029/2020JF005714

Longuet-Higgins, M. S., & Jeffreys, H. (1950). A theory of the origin of microseisms. *Philosophical Transactions of the Royal Society of London. Series A, Mathematical and Physical Sciences*, *243*(857), 1–35. https://doi.org/10.1098/rsta.1950.0012

Lunedei, E., & Albarello, D. (2009). On the seismic noise wavefield in a weakly dissipative layered Earth. *Geophysical Journal International*, *177*(3), 1001–1014. https://doi.org/10.1111/j.1365-246X.2008.04062.x

Lunedei, E., & Albarello, D. (2010). Theoretical HVSR curves from full wavefield modelling of ambient vibrations in a weakly dissipative layered Earth. *Geophysical Journal International*, *181*(2), 1093–1108. https://doi.org/10.1111/j.1365-246X.2010.04560.x

Lunedei, E., & Albarello, D. (2015). Horizontal-to-vertical spectral ratios from a full-wavefield model of ambient vibrations generated by a distribution of spatially correlated surface sources. *Geophysical Journal International*, *201*(2), 1142–1155. https://doi.org/10.1093/gji/ggv046

Lunedei, E., & Albarello, D. (2021). Synthetic spectral structure of the seismic ambient vibrations generated by a distribution of superficial random sources with a finite extension. *Soil Dynamics and Earthquake Engineering*, *151*, 106949. https://doi.org/10.1016/j.soildyn.2021.106949

Lunedei, E., & Malischewsky, P. (2015). A review and some new issues on the theory of the H/V technique for ambient vibrations. In *Perspectives on European earthquake engineering and seismology* (Vol. 39, pp. 371–394). Springer.

MacGregor, J. A., Boisvert, L. N., Medley, B., Petty, A. A., Harbeck, J. P., Bell, R. E., et al. (2021). The scientific legacy of NASA's operation IceBridge. *Reviews of Geophysics*, *59*(2), e2020RG000712. https://doi.org/10.1029/2020RG000712

Matsushima, S., Hirokawa, T., De Martin, F., Kawase, H., & Sánchez-Sesma, F. J. (2014). The effect of lateral heterogeneity on horizontal-to-vertical spectral ratio of microtremors inferred from observation and synthetics. *Bulletin of the Seismological Society of America*, *104*(1), 381–393. https://doi.org/10.1785/0120120321

Matsushima, S., Kosaka, H., & Kawase, H. (2017). Directionally dependent horizontal-to-vertical spectral ratios of microtremors at Onahama, Fukushima, Japan. *Earth Planets and Space*, *69*(1), 96. https://doi.org/10.1186/s40623-017-0680-9

Mavko, G., Mukerji, T., & Dvorkin, J. (2020). *The rock physics handbook*. Cambridge University Press.

McCormack, F. S., Warner, R. C., Seroussi, H., Dow, C. F., Roberts, J. L., & Treverrow, A. (2022). Modeling the deformation regime of Thwaites Glacier, West Antarctica, using a simple flow relation for ice anisotropy (ESTAR). *Journal of Geophysical Research, Earth Surface*, *127*(3), e2021JF006332. https://doi.org/10.1029/2021JF006332

Megies, T., Beyreuther, M., Barsch, R., Krischer, L., & Wassermann, J. (2011). ObsPy – What can it do for data centers and observatories? *Annals of Geophysics*, *54*(1), 47–58. https://doi.org/10.4401/ag-4838

Mi, B., Hu, Y., Xia, J., & Socco, L. V. (2019). Estimation of horizontal-to-vertical spectral ratios (ellipticity) of Rayleigh waves from multistation active-seismic records. *Geophysics*, *84*(6), EN81–EN92. https://doi.org/10.1190/geo2018-0651.1

Mi, B., Xia, J., Shen, C., & Wang, L. (2018). Dispersion energy analysis of Rayleigh and love waves in the presence of low-velocity layers in near-surface seismic surveys. *Surveys in Geophysics*, *39*(2), 271–288. https://doi.org/10.1007/s10712-017-9440-4

Millan, R., Mouginot, J., Rabatel, A., & Morlighem, M. (2022). Ice velocity and thickness of the world's glaciers. *Nature Geoscience*, *15*(2), 124–129. https://doi.org/10.1038/s41561-021-00885-z

Molnar, S., Sirohey, A., Assaf, J., Bard, P.-Y., Castellaro, S., Cornou, C., et al. (2022). A review of the microtremor horizontal-to-vertical spectral ratio (mHVSR) method. *Journal of Seismology*, *26*(4), 1–33. https://doi.org/10.1007/s10950-021-10062-9

Mordret, A., Mikesell, T. D., Harig, C., Lipovsky, B. P., & Prieto, G. A. (2016). Monitoring southwest Greenland's ice sheet melt with ambient seismic noise. *Science Advances*, *2*(5), e1501538. https://doi.org/10.1126/sciadv.1501538

Morlighem, M. (2022). MEaSUREs BedMachine Antarctica (version 3) [Dataset]. *NASA National Snow and Ice Data Center Distributed Active Archive Center*. https://doi.org/10.5067/FPSU0V1MWUB6

Morlighem, M., Rignot, E., Binder, T., Blankenship, D., Drews, R., Eagles, G., et al. (2020). Deep glacial troughs and stabilizing ridges unveiled beneath the margins of the Antarctic Ice Sheet. *Nature Geoscience*, *13*(2), 132–137. https://doi.org/10.1038/s41561-019-0510-8

Mouginot, J., Scheuchl, B., & Rignot, E. (2017). MEaSUREs Antarctic boundaries for IPY 2007–2009 from satellite radar (version 2) [Dataset]. *NASA National Snow and Ice Data Center Distributed Active Archive Center*. https://doi.org/10.5067/axe4121732ad

Mucciarelli, M., Gallipoli, M. R., & Arcieri, M. (2003). The stability of the horizontal-to-vertical spectral ratio of triggered noise and earthquake recordings. *Bulletin of the Seismological Society of America*, *93*(3), 1407–1412. https://doi.org/10.1785/0120020213

Mulargia, F., & Castellaro, S. (2016). HVSR deep mapping tested down to ∼1.8km in Po Plane Valley, Italy. *Physics of the Earth and Planetary Interiors*, *261*, 17–23. https://doi.org/10.1016/j.pepi.2016.08.002

Muto, A., Anandakrishnan, S., Alley, R. B., Horgan, H. J., Parizek, B. R., Koellner, S., et al. (2019). Relating bed character and subglacial morphology using seismic data from Thwaites Glacier, West Antarctica. *Earth and Planetary Science Letters*, *507*, 199–206. https://doi.org/10.1016/j.epsl.2018.12.008

Nakamura, Y. (1989). A method for dynamic characteristics estimation of subsurface using microtremor on the ground surface. *Railway Technical Research Institute, Quarterly Reports*, *30*(1), 25–33.

Nakamura, Y. (2019). What is the Nakamura method? *Seismological Research Letters*, *90*(4), 1437–1443. https://doi.org/10.1785/0220180376

Nakata, N., Gualtieri, L., & Fichtner, A. (2019). *Seismic ambient noise*. Cambridge University Press. https://doi.org/10.1017/9781108264808

Noble, T. L., Rohling, E. J., Aitken, A. R. A., Bostock, H. C. E. A., Chase, Z., Gomez, N., et al. (2020). The sensitivity of the Antarctic ice sheet to a changing climate: Past, present, and future. *Reviews of Geophysics*, *58*(4), e2019RG000663. https://doi.org/10.1029/2019RG000663

Nogoshi, M., & Igarashi, T. (1971). On the amplitude characteristics of microtremor (part 2). *Journal of the Seismological Society of Japan*, *24*(1), 26–40. https://doi.org/10.4294/zisin1948.24.1_26

Otosaka, I. N., Shepherd, A., Ivins, E. R., Schlegel, N.-J., Amory, C., van den Broeke, M. R., et al. (2023). Mass balance of the Greenland and Antarctic ice sheets from 1992 to 2020. *Earth System Science Data*, *15*(4), 1597–1616. https://doi.org/10.5194/essd-15-1597-2023

Oubaiche, E. H., Chatelain, J., Hellel, M., Wathelet, M., Machane, D., Bensalem, R., & Bouguern, A. (2016). The relationship between ambient vibration H/V and SH transfer function: Some experimental results. *Seismological Research Letters*, *87*(5), 1112–1119. https://doi.org/10.1785/0220160113

Paolucci, E., Albarello, D., D'Amico, S., Lunedei, E., Martelli, L., Mucciarelli, M., & Pileggi, D. (2015). A large scale ambient vibration survey in the area damaged by May—June 2012 seismic sequence in Emilia Romagna, Italy. *Bulletin of Earthquake Engineering*, *13*(11), 3187–3206. https://doi.org/10.1007/s10518-015-9767-5

Paolucci, E., Tanzini, A., & Albarello, D. (2023). From HVSR to site SH response function: Potentiality and pitfalls inferred by 1D physical modelling. *Soil Dynamics and Earthquake Engineering*, *165*, 107703. https://doi.org/10.1016/j.soildyn.2022.107703

Parkinson, C. L., & Cavalieri, D. J. (2012). Antarctic sea ice variability and trends, 1979–2010. *The Cryosphere*, *6*(4), 871–880. https://doi.org/10.5194/tc-6-871-2012

Parolai, S., Bormann, P., & Milkereit, C. (2002). New relationship between Vs, thickness of sediments, and resonance frequency calculated by the H/V ratio of seismic noise for the Cologne Area (Germany). *Bulletin of the Seismological Society of America*, *92*(6), 2521–2527. https://doi.org/10.1785/0120010248

Parolai, S., Picozzi, M., Strollo, A., Pilz, M., Di Giacomo, D., Liss, B., & Bindi, D. (2009). Are transients carrying useful information for estimating H/V spectral ratios? In *Increasing seismic safety by combining engineering technologies and seismological data* (pp. 17–31). Springer. https://doi.org/10.1007/978-1-4020-9196-4_3

Parolai, S., Richwalski, S. M., Milkereit, C., & Bormann, P. (2004). Assessment of the stability of H/V spectral ratios from ambient noise and comparison with earthquake data in the Cologne Area (Germany). *Tectonophysics*, *390*(1), 57–73. https://doi.org/10.1016/j.tecto.2004.03.024

Pattyn, F., & Morlighem, M. (2020). The uncertain future of the Antarctic ice sheet. *Science*, *367*(6484), 1331–1335. https://doi.org/10.1126/science.aaz5487

Paxman, G. J. G., Jamieson, S. S. R., Ferraccioli, F., Jordan, T. A., Bentley, M. J., Ross, N., et al. (2019). Subglacial geology and geomorphology of the Pensacola-Pole Basin, East Antarctica. *Geochemistry, Geophysics, Geosystems*, *20*(6), 2786–2807. https://doi.org/10.1029/2018GC008126

Pearce, E., Booth, A. D., Rost, S., Sava, P., Konuk, T., Brisbourne, A., et al. (2023). Characterising ice slabs in firn using seismic full waveform inversion, a sensitivity study. *Journal of Glaciology*, *69*(277), 1–15. https://doi.org/10.1017/jog.2023.30

Pearce, E., Zigone, D., Hofstede, C., Fichtner, A., Rimpot, J., Rasmussen, S. O., et al. (2024). Firn seismic anisotropy in the Northeast Greenland Ice Stream from ambient-noise surface waves. *The Cryosphere*, *18*(10), 4917–4932. https://doi.org/10.5194/tc-18-4917-2024

Peters, L. E., Anandakrishnan, S., Alley, R. B., & Voigt, D. E. (2012). Seismic attenuation in glacial ice: A proxy for englacial temperature. *Journal of Geophysical Research, Earth Surface*, *117*(F2), F02008. https://doi.org/10.1029/2011JF002201

Phạm, T.-S., & Tkalčić, H. (2018). Antarctic ice properties revealed from teleseismic P wave coda autocorrelation. *Journal of Geophysical Research: Solid Earth*, *123*(9), 7896–7912. https://doi.org/10.1029/2018JB016115

Picotti, S., Francese, R., Giorgi, M., Pettenati, F., & Carcione, C. M. (2017). Estimation of glacier thicknesses and basal properties using the horizontal-to-vertical component spectral ratio (HVSR) technique from passive seismic data. *Journal of Glaciology*, *63*(238), 229–248. https://doi.org/10.1017/jog.2016.135

Podolskiy, E. A., & Walter, F. (2016). Cryoseismology. *Reviews of Geophysics*, *54*(4), 708–758. https://doi.org/10.1002/2016RG000526

Pratt, M. J., Wiens, D. A., Winberry, J. P., Anandakrishnan, S., & Euler, G. G. (2017). Implications of sea ice on Southern Ocean microseisms detected by a seismic array in West Antarctica. *Geophysical Journal International*, *209*(1), 492–507. https://doi.org/10.1093/gji/ggx007

Pritchard, H. D., Fretwell, P. T., Fremand, A. C., Bodart, J. A., Kirkham, J. D., Aitken, A., et al. (2025). Bedmap3 updated ice bed, surface and thickness gridded datasets for Antarctica. *Scientific Data*, *12*(1), 414. https://doi.org/10.1038/s41597-025-04672-y

Reading, A. M., Stål, T., Halpin, J. A., Lösing, M., Ebbing, J., Shen, W., et al. (2022). Antarctic geothermal heat flow and its implications for tectonics and ice sheets. *Nature Reviews Earth & Environment*, *3*(12), 814–831. https://doi.org/10.1038/s43017-022-00348-y

Rignot, E., Mouginot, J., Scheuchl, B., van den Broeke, M., van Wessem, M. J., & Morlighem, M. (2019). Four decades of Antarctic ice sheet mass balance from 1979–2017. *Proceedings of the National Academy of Sciences*, *116*(4), 1095–1103. https://doi.org/10.1073/pnas.1812883116

Rigo, A., Sokos, E., Lefils, V., & Briole, P. (2021). Seasonal variations in amplitudes and resonance frequencies of the HVSR amplification peaks linked to groundwater. *Geophysical Journal International*, *226*(1), 1–13. https://doi.org/10.1093/gji/ggab086

Ritz, C., Edwards, T. L., Durand, G., Payne, A. J., Peyaud, V., & Hindmarsh, R. C. A. (2015). Potential sea-level rise from Antarctic ice-sheet instability constrained by observations. *Nature*, *528*(7580), 115–118. https://doi.org/10.1038/nature16147

Robel, A. A., Sim, S. J., Meyer, C., Siegfried, M. R., & Gustafson, C. D. (2023). Contemporary ice sheet thinning drives subglacial groundwater exfiltration with potential feedbacks on glacier flow. *Science Advances*, *9*(33), eadh3693. https://doi.org/10.1126/sciadv.adh3693

Sánchez-Sesma, F. J., Rodríguez, M., Iturrarán-Viveros, U., Luzón, F., Campillo, M., Margerin, L., et al. (2011). A theory for microtremor H/V spectral ratio: Application for a layered medium. *Geophysical Journal International*, *186*(1), 221–225. https://doi.org/10.1111/j.1365-246X.2011.05064.x

Schön, J. H. (2015). *Physical properties of rocks: Fundamentals and principles of petrophysics* (Vol. 65). Elsevier.

Schroeder, D. M., Bingham, R. G., Blankenship, D. D., Christianson, K., Eisen, O., Flowers, G. E., et al. (2020). Five decades of radioglaciology. *Annals of Glaciology*, *61*(81), 1–13. https://doi.org/10.1017/aog.2020.11

Seivane, H., García-Jerez, A., Navarro, M., Molina, L., & Navarro-Martínez, F. (2022). On the use of the microtremor HVSR for tracking velocity changes: A case study in Campo de Dalías Basin (SE Spain). *Geophysical Journal International*, *230*(1), 542–564. https://doi.org/10.1093/gji/ggac064

Sergeant, A., Stutzmann, E., Maggi, A., Schimmel, M., Ardhuin, F., & Obrebski, M. (2013). Frequency-dependent noise sources in the North Atlantic Ocean. *Geochemistry, Geophysics, Geosystems*, *14*(12), 5341–5353. https://doi.org/10.1002/2013GC004905

Smith, A. M., Bentley, C. R., Bingham, R. G., & Jordan, T. A. (2012). Rapid subglacial erosion beneath Pine Island Glacier, West Antarctica. *Geophysical Research Letters*, *39*(12). https://doi.org/10.1029/2012GL051651

Smith, A. M., Murray, T., Nicholls, K., Makinson, K., Aðalgeirsdóttir, G., Behar, A., & Vaughan, D. (2007). Rapid erosion, drumlin formation, and changing hydrology beneath an Antarctic ice stream. *Geology*, *35*(2), 127–130. https://doi.org/10.1130/G23036A.1

Stevens, N. T., Roland, C. J., Zoet, L. K., Alley, R. B., Hansen, D. D., & Schwans, E. (2023). Multi-decadal basal slip enhancement at Saskatchewan Glacier, Canadian Rocky Mountains. *Journal of Glaciology*, *69*(273), 71–86. https://doi.org/10.1017/jog.2022.45

Stutzmann, E., Ardhuin, F., Schimmel, M., Mangeney, A., & Patau, G. (2012). Modelling long-term seismic noise in various environments. *Geophysical Journal International*, *191*(2), 707–722. https://doi.org/10.1111/j.1365-246X.2012.05638.x

Stutzmann, E., Schimmel, M., Patau, G., & Maggi, A. (2009). Global climate imprint on seismic noise. *Geochemistry, Geophysics, Geosystems*, *10*(11). https://doi.org/10.1029/2009GC002619

The Matplotlib Development Team. (2025). Matplotlib: Visualization with python: February 27, 2025 release (version 3.10.1) [Software]. *Zenodo*. https://doi.org/10.5281/zenodo.14940554

The Met Office. (2010). Cartopy: A cartographic Python library with a Matplotlib interface. (Tech. Rep.).

The ObsPy Development Team. (2025). ObsPy: April 30, 2025 release (version 1.4.2) [Software]. *Zenodo*. https://doi.org/10.5281/zenodo.15309143

Toksoz, M. N., Cheng, C. H., & Timur, A. (1976). Velocities of seismic waves in porous rocks. *Geophysics*, *41*(4), 621–645. https://doi.org/10.1190/1.1440639

Toksöz, M. N., Johnston, D. H., & Timur, A. (1979). Attenuation of seismic waves in dry and saturated rocks: I. laboratory measurements. *Geophysics*, *44*(4), 681–690. https://doi.org/10.1190/1.1440969

Tsai, V. C., & McNamara, D. E. (2011). Quantifying the influence of sea ice on ocean microseism using observations from the Bering Sea, Alaska. *Geophysical Research Letters*, *38*(22). https://doi.org/10.1029/2011GL049791

Tuan, T. T., Scherbaum, F., & Malischewsky, P. G. (2011). On the relationship of peaks and troughs of the ellipticity (H/V) of Rayleigh waves and the transmission response of single layer over half-space models. *Geophysical Journal International*, *184*(2), 793–800. https://doi.org/10.1111/j.1365-246X.2010.04863.x

Turner, R. J., Gal, M., Hemer, M. A., & Reading, A. M. (2020). Impacts of the cryosphere and atmosphere on observed microseisms generated in the southern ocean. *Journal of Geophysical Research, Earth Surface*, *125*(2), e2019JF005354. https://doi.org/10.1029/2019JF005354

van den Broeke, M. (2008). Depth and density of the Antarctic firn layer. *Arctic Antarctic and Alpine Research*, *40*(2), 432–438. https://doi.org/10.1657/1523-0430(07-021)[BROEKE]2.0.CO;2

van Ginkel, J., Walter, F., Lindner, F., Hallo, M., Huss, M., & Fäh, D. (2025). Spectral characteristics of seismic ambient vibrations reveal changes in the subglacial environment of Glacier de la Plaine Morte, Switzerland. *The Cryosphere*, *19*(3), 1469–1490. https://doi.org/10.5194/tc-19-1469-2025

Vantassel, J. P. (2021). Jpvantassel/hvsrpy: October 12, 2021 release (version 1.0.0) [Software]. *Zenodo*. https://doi.org/10.5281/zenodo.5563211

Vantassel, J. P. (2025). Hvsrpy: An open-source python package for microtremor and earthquake horizontal-to-vertical spectral ratio processing. *Seismological Research Letters*, *96*(4), 2671–2682. https://doi.org/10.1785/0220240395

Velicogna, I., Mohajerani, Y., A, G., Landerer, F., Mouginot, J., Noel, B., et al. (2020). Continuity of ice sheet mass loss in Greenland and Antarctica from the GRACE and GRACE follow-on missions. *Geophysical Research Letters*, *47*(8), e2020GL087291. https://doi.org/10.1029/2020GL087291

Walter, F., Chaput, J., & Lüthi, M. P. (2014). Thick sediments beneath Greenland's ablation zone and their potential role in future ice sheet dynamics. *Geology*, *42*(6), 487–490. https://doi.org/10.1130/g35492.1

Wathelet, M. (2008). An improved neighborhood algorithm: Parameter conditions and dynamic scaling. *Geophysical Research Letters*, *35*(9). https://doi.org/10.1029/2008GL033256

Whitehouse, P. L., Gomez, N., King, M. A., & Wiens, D. A. (2019). Solid Earth change and the evolution of the Antarctic ice sheet. *Nature Communications*, *10*(1), 503. https://doi.org/10.1038/s41467-018-08068-y

Winter, K., Woodward, J., Ross, N., Dunning, S. A., Hein, A. S., Westoby, M. J., et al. (2019). Radar-detected englacial debris in the West Antarctic ice sheet. *Geophysical Research Letters*, *46*(17–18), 10454–10462. https://doi.org/10.1029/2019GL084012

Wittlinger, G., & Farra, V. (2012). Observation of low shear wave velocity at the base of the polar ice sheets: Evidence for enhanced anisotropy. *Geophysical Journal International*, *190*(1), 391–405. https://doi.org/10.1111/j.1365-246X.2012.05474.x

Wittlinger, G., & Farra, V. (2015). Evidence of unfrozen liquids and seismic anisotropy at the base of the polar ice sheets. *Polar Science*, *9*(1), 66–79. https://doi.org/10.1016/j.polar.2014.07.006

Yan, P., Li, Z., Li, F., Yang, Y., Hao, W., & Bao, F. (2018). Antarctic ice sheet thickness estimation using the horizontal-to-vertical spectral ratio method with single-station seismic ambient noise. *The Cryosphere*, *12*(2), 795–810. https://doi.org/10.5194/tc-12-795-2018

Yang, Y., & Ritzwoller, M. H. (2008). Characteristics of ambient seismic noise as a source for surface wave tomography. *Geochemistry, Geophysics, Geosystems*, *9*(2). https://doi.org/10.1029/2007GC001814

Yin, Z., Zuo, C., MacKie, E. J., & Caers, J. (2022). Mapping high-resolution basal topography of West Antarctica from radar data using non-stationary multiple-point geostatistics (mps-bedmappingv1). *Geoscientific Model Development*, *15*(4), 1477–1497. https://doi.org/10.5194/gmd-15-1477-2022

Zhan, Z. (2019). Seismic noise interferometry reveals transverse drainage configuration beneath the surging Bering Glacier. *Geophysical Research Letters*, *46*(9), 4747–4756. https://doi.org/10.1029/2019GL082411

Zhang, Z., & Olugboji, T. (2023). Lithospheric imaging through reverberant layers: Sediments, oceans, and glaciers. *Journal of Geophysical Research: Solid Earth*, *128*(5), e2022JB026348. https://doi.org/10.1029/2022JB026348

Zhao, C., Gladstone, R., Zwinger, T., Gillet-Chaulet, F., Wang, Y., Caillet, J., et al. (2025). Subglacial water amplifies Antarctic contributions to sea-level rise. *Nature Communications*, *16*(1), 3187. https://doi.org/10.1038/s41467-025-58375-4